creative commons
COMMONS DEED

저작자표시-비영리-변경금지 2.0 대한민국

이용자는 아래의 조건을 따르는 경우에 한하여 자유롭게

- 이 저작물을 복제, 배포, 전송, 전시, 공연 및 방송할 수 있습니다.

다음과 같은 조건을 따라야 합니다:

저작자표시. 귀하는 원저작자를 표시하여야 합니다.

비영리. 귀하는 이 저작물을 영리 목적으로 이용할 수 없습니다.

변경금지. 귀하는 이 저작물을 개작, 변형 또는 가공할 수 없습니다.

- 귀하는, 이 저작물의 재이용이나 배포의 경우, 이 저작물에 적용된 이용허락조건을 명확하게 나타내어야 합니다.
- 저작권자로부터 별도의 허가를 받으면 이러한 조건들은 적용되지 않습니다.

저작권법에 따른 이용자의 권리는 위의 내용에 의하여 영향을 받지 않습니다.

이것은 이용허락규약(Legal Code)을 이해하기 쉽게 요약한 것입니다.

Disclaimer

dCollection

M.S. THESIS

Migration of Radiative Gas Giants with GIZMO

GIZMO를 이용한 복사성 목성형 행성들의 이주 현상 수치 실험

BY

YANG SEUNG-WON

AUGUST 2019

ASTRONOMY PROGRAM
DEPARTMENT OF PHYSICS AND ASTRONOMY
SEOUL NATIONAL UNIVERSITY

M.S. THESIS

Migration of Radiative Gas Giants with GIZMO

GIZMO를 이용한 복사성 목성형 행성들의 이주 현상 수치 실험

BY

YANG SEUNG-WON

AUGUST 2019

ASTRONOMY PROGRAM
DEPARTMENT OF PHYSICS AND ASTRONOMY
SEOUL NATIONAL UNIVERSITY

Migration of Radiative Gas Giants with GIZMO

GIZMO를 이용한 복사성 목성형 행성들의 이주 현상 수치 실험

지도교수 김웅태
이 논문을 이학석사 학위논문으로 제출함

2019년 8월

서울대학교 대학원

물리·천문학부 천문학전공

양승원

양승원의 이학석사 학위 논문을 인준함

2019년 8월

위 원 장:	구 본 철	(인)
부위원장:	김 웅 태	(인)
위 원:	윤 성 철	(인)

Abstract

A gas giant formed in a massive protoplanetary disk via gravitational instability grows in mass by accreting the surrounding disk material and simultaneously migrates due to its tidal interaction with the disk. Since the accretion flow onto the planet is enhanced for colder material within the Hill sphere, the planet migration is dominantly affected by both planet mass and disk cooling rate. Previous numerical studies on the migration of accreting protoplanets predicted the formation of brown dwarfs or low-mass stars rather than gas giants. In this thesis, we perform three-dimensional hydrodynamic simulations using GIZMO (Hopkins 2015) to investigate the evolution of a giant planet in a massive protoplanetary disk by allowing for radiative feedback resulting from gas accretion onto the planet in the framework of the β-cooling model suggested by Gammie (2001). We find that a protoplanet in a massive protoplanetary disk rapidly migrates inward and gradually stalls as the disk opens a gap. The accretion rate is measured to be higher for a heavier planet and/or a colder disk. In general, the presence of radiative feedback tends to suppress the accretion rate onto a planet and delay gap opening, thereby keeping the final planet mass below the brown dwarf regime. We discuss our results in comparison with the previous numerical studies.

keywords: Numerical simulation: Hydrodynamics — Radiative Feedback, Protoplanetary disk: Accretion disk — Planet — Planet-disk interaction — Planet migration

student number: 2016-23078

Contents

List of Tables

List of Figures

Chapter 1

Introduction

The theory of formation and evolution of the planetary system aims to understand our solar system consisting of terrestrial planets and gas giants. An early theory of planet formation suggested a scenario of core-accretion (e.g., Safronov 1969; Goldreich & Ward 1973; Hayashi et al. 1985; Pollack et al. 1996) describing the growth of rocky body as hierarchical collisional coagulation among planetesimals but failed due to such a long evolution timescale compared with lifetime of the protoplanetary disk. Also, the core accretion model cannot explain metallicity

An alternative scenario for planet formation is gravitational instability (e.g., Cameron 1978; Boss 1997) in a massive protoplanetary disk. If the disk locally cold and dense enough to satisfy the Toomre's instability criterion (Toomre 1964) which is

$$Q_{\rm T} = \frac{c_{\rm s}\Omega_{\rm K}}{\pi G\Sigma} \lesssim 1 \tag{1.1}$$

for razor-thin Keplerian disk, where $c_{\rm s}$ and $\Omega_{\rm K}$ are sound speed and Keplerian angular frequency, it is likely able to fragment into dense clumps quickly (within a few thousand years). However, the Tommre instability generally invokes linear instability on the disk first rather than triggers local fragmentation. The unstable disk forms non-axisymmetric structure like spiral arms transporting disk angular momentum outward by a gravitational torque (Boss 1988; Bate 1998). So disk material falls inward

along the spiral arms by releasing its energy as gravitational heating onto surrounding (Armitage 2015). Consequently, the Toomre instability results in both increase of temperature at overall outer disk region and subsequently stabilizes disk before local instability occurs (i.e., $Q_{\rm T} > 1$).

Against thermal expansion by the gravitational heating, we understand the disk requires an efficient cooling process for the protoplanet to be formed from gravitational instability. Without considering details on the cooling process, Gammie (2001) introduced a cooling rate parameterized with a local dynamical timescale to be $t_{\rm cool} = \beta\Omega_{\rm K}^{-1}$. So the Gammie's prescription cools down gas flow, so that

$$\left.\frac{\partial u}{\partial t}\right|_{\rm cool} = \frac{u}{t_{\rm cool}} = \frac{u\Omega_{\rm K}}{\beta}. \tag{1.2}$$

In his paper, a critical value of β to trigger local instability was estimated at $\beta_{\rm crit} = 3$ with adiabatic index $\gamma = 2$, but depending upon initial disk properties and different simulation domains, the threshold changes in a wide range (e.g., Meru & Bate 2010; 2012; Paardekooper et al. 2011; Klee et al. 2017). On the other hand, the radiative transfer method in the SPH simulation with diffusion approximation of Stamatellos et al. (2007) dealing with the radiative process of chemicals, ices, and dust components replaced model-dependent β-cooling approximation. In his later studies, mass growth of the planet was shown a quite high accretion rate (Stamatellos & Whiteworth 2009; Stamatellos 2015; Stamatellos & Inutsuka 2018), which seems to estimate relatively cold disk temperature compared with $\beta \lesssim 3$ in β-cooling models.

In any method of radiative transfer, the unstable disk can be supported by a rapid cooling process, and therefore disk fragmentation occurs at the intermediate disk region where it exhibits sufficient density and low temperature. Further internal cooling of the clumps leads to formation of protoplanet. The gravitational instability predicts the initial mass of protoplanet at $(1 - 10\,M_{\rm J})$ based on a criterion of opacity-limited fragmentation (e.g., Rees 1976; Silk 1977; Boss 1988; Masunaga et al. 1998; Bate 2004; Rafikov 2005; Whitworth 2005; Whitworth & Stamatellos 2006; Boley et al. 2010; Kratter et al. 2010; Forgan & Rice 2011, 2013a; Boss 2011; Rogers & Wadsley

2012; Tsukamoto et al. 2015).

Formation of the protoplanet leads to gravitational interaction between the planet and the disk, allowing for the planet to migrate inward (Goldreich & Tremaine 1979; 1980) and for the disk to open a gap (Tanaka et al. 2002). This evolution process in the protoplanetary disk with protoplanet is called the planet migration. During migration, the disk-planet interaction triggers linear gravitational instability forming spiral arms around the planet and exerts gravitational torque to the disk in forms of co-rotational and Lindblad ones. Here the co-rotational torque takes the role of planet accretion, and Lindblad torque causes disk gap opening and orbital evolution of the planet.

A shearing disk flow around the planet orbit is affected by co-rotational torque caused by the gravitational attraction of the planet. Due to the co-rotational torque, the shearing flow of the inner disk gains angular momentum and shifts outer disk along the spiral arm and also vice verse. The orbital switching between inner and outer shearing flows appears with horseshoe-orbit. On the other hand, the shearing flow nearby the planet is captured into the Hill sphere. The disk material within the Hill sphere develops circumplanetary disk subject to be accreted onto the planet via viscous dissipation. So accretion rate onto the planet depends on planet mass and thermal properties around the planet. A Lindblad resonance on the planet exerts negative torque that makes the planet generally tend to lose its angular momentum and to migrate inward. We note that the Lindblad resonance torque is enhanced with mass growth of the planet. In the role of Lindblad torque on gap opening, the disk cannot open a gap since the Lindblad torque rivals viscous dissipation before the planet achieves sufficient mass growth. Once the Lindblad torque surpasses viscous dissipation with mass growth of the planet, it repels disk material around the planet orbit and forms a disk gap. After the disk ends gap opening, the motion of the planet is locked within the gap and then gradually stalls orbital evolution.

As the consequences of the planet migration, we expect planet gains mass and alters its orbital radius, forming a gap or spiral arms on the disk. Early numerical

studies on the evolution of protoplanet with no accretion process showed rapid inward migration rate like type I migration without slowing down, and therefore the planet is distroyed via stellar irradiation and tidal torque (Baruteau et al. 2011; Michael et al. 2011; Malik et al. 2015). The follow-up studies allowing accretion onto the planet found the planet can survive by stalling migration because mass growth of the planet is eligible to make the disk open gap. However, the commonly measured high accretion rate makes the planet evolve into a brown dwarf or a low-mass star rather than a gas giant (Stamatellos & Whiteworth 2009; Zhu et al 2012; Stamatellos 2015; Stamatellos & Inutsuka 2018; Humphries & Nayakshin 2018). The outward migration was detected in typical researches. Cloutier & Lin (2013) showed additional torque from gap edges based on gravitational instability of the unstable disk exerts outward torque on the planet and makes it move outward after gap opening. Also, the inward migration slows and turns outward if the planet rapidly achieves sufficient mass growth (Stamatellos 2015; Stamatellos & Inutsuka 2018). To solve the problems of previous studies, an alternative theory on the planet evolution was suggested by Nayakshin (2017). He described diverse types of planets (e.g., largely terrestrial planet and gas giant) is able to be formed via gravitational instability in the massive protoplanetary disk and via further mass evolution of tidal disruption of the host star. His study well explained the population of Jovian planets or Brown dwarf matched with observation. However, the origin of eccentric Jupiters (exhibit Jovian masses and very eccentric orbit) and Hot Jupiters (exist very nearby the host star at $R_{\rm p} \lesssim 1\,{\rm AU}$ but have the massive bodies of $M_{\rm p} \gtrsim 10\,M_{\rm J}$) is still a mystery.

Not only the gravitational interaction between disk and planet but various internal processes (e.g., irradiation, magnetic field, and dust physics) influence the way of planet migration. A primary factor that affects the dynamic and thermal evolution of the protoplanetary disk is considered to be the radiative process of star and planet. The protoplanetary disk orbiting the protostar suffers from stellar irradiation that governs disk temperature. Even the strong stellar irradiation ($L_* \gtrsim 1\,L_\odot$) can ionize disk sur-

face and disperse away from the surface as outflow, i.e., photoevaporation (Pollack et al. 1996; Hubickyj et al. 2005). While self-luminosity of the protoplanet is negligible compared with the protostar (Helled et al. 2011; Nayakshin 2015), the accreting protoplanet emits accreted energy as radiation estimated at a few percentages to a few tenths of solar luminosity (Stamatellos & Inutsuka 2018). The planet radiative feedback makes surrounding disk material not to readily cool down to be accreted onto the planet and delays gap opening by enhancing viscous dissipation (Nayakshin & Cha 2013; Stamatellos 2015; Ben ıtez-Llambay et al. 2015; Stamatellos & Inutsuka 2018). There needs more investigation, but the magnetic field induced from ionized components complicates the situation of planet migration (Wardle 2007, Gressel et al 2013). The magnetic field generates turbulence acting as viscosity in the disk and disperses disk material via magneto-outflow like photoevaporation. Evolution of the dust particles during planet migration may explain diverse chemical types of the gas giant. Humphries and Nayakshin (2018) found an inverse correlation between the planet mass and its metallicity although coupling between dust and gas do not change planet evolution. There is large uncertainty in the role of protoplanetary dust on the planet evolution yet, but we already understand metallicity depending on the distribution and population of dust particles determines disk opacity which relates with the efficiency of radiative cooling (Helled et al. 2013).

In this work, we have newly developed numerical task bench with the GIZMO code (Hopkins 2015) to investigate planet evolution via migration. The GIZMO code features a second-order accurate hydrodynamics code based on a kernel discretization of the volume coupled to a high-order matrix gradient estimator and a Riemann solver acting over the volume overlap. This numerical scheme exactly showed conservative physical quantities (e.g., angular momentum) and modified accuracy in the sub-sonic flow. We expect the GIZMO using realistic viscosity term rather than artificial prescription in other SPH methods significantly increase numerical accuracy on dealing with viscous transport of disk angular momentum. In addition, the GIZMO solved a

problem of non-convergent critical cooling rate for disk fragment in previous numerical studies (Deng et al. 2017). Using the numerical setup with the GIZMO, we have performed the twenty simulations of planet migration in wide parameter spaces with different initial mass and orbital radius of protoplanet, cooling rate with β coefficient, and strength of planet radiative feedback. From our simulation results, we mainly aim to understand how the protoplanet considered to be formed in massive protoplanetary disk evolves in various situations and to find the correlations between observables and simulation results. Also, we will discuss the results by comparing with previous numerical studies which used different numerical method and assumed different disk properties and internal physics.

We carry out the simulation with a toy model which initially set protoplanet corotates with dynamically relaxed disk flow at a certain distance away from the central star. Disk temperature is determined by stellar irradiation and cooling source provided by β-cooling model but locally heated by planet irradiation if it is accreting disk material as feedback. Initial setup for surface density and temperature profiles of the disk yields gravitationally stable disk ($Q_{\mathrm{T,init}} \gtrsim 1.5$), which do not make the protoplanetary disk form protoplanets via gravitational instability anymore. The most worrying shortcoming of this initial setup compared with the realistic situation right-after protoplanet formation is the disk is likely unstable far from the sub-Keplerian disk of a toy model. Moreover, this simulation even only considers a single governing gas giant, ignoring the following formation of another protoplanet. Nevertheless, we believe simulation with the toy model will suggest insight for understanding the physics of planet migration through the simplest numerical setups.

We describe the internal structure and dynamics of a protoplanetary disk in detail in **Chapter 2** and **3**. Following these, we constrain an initial setup for simulations. We demonstrate the numerical schemes for the accretion process, the planet radiative feedback, and thermal evolution in **Chapter 4** and how these are established in the GIZMO. In **Chapter 5**, we first introduce simulations of Bondi-accretion test and

migration of radiative protoplanet. Bondi-accretion test confirms the validity of our numerical scheme. In **Chapther 6**, we summarize and discuss the simulation results focusing on properties of the planet, circumplanetary disk, and disk gap resulting from the migration. In this chapter, we will show the meaning and implication of this work compared with previous numerical works. At the end of this paper (**Chapter 7**), we append additional figures and tables used in previous chapters.

Chapter 2

Disk Structure

Direct imaging of the protoplanetary disk and modeling of spectral energy distribution provides basic physical quantities of the disk such as surface density, temperature, and velocity distributions. Here the observed velocity profile is considered to be a sub-Keplerian motion that implies the protoplanetary disk may be in quasi-hydrostatic equilibrium. The observation, however, has an inherent limitation to detect the disk interior, so that the three-dimensional structure and chemical distribution are uncertain, but we only guess the disk is vertically flaring from excess emission at far IR (Kenyon & Hartmann 1987). In this chapter, we propose the vertical structure of the disk using condition for hydrostatic equilibrium.

2.1 Surface Density

The protoplanetary disk (hereafter PPD) features a remarkable infrared spectrum due to dust emission in spectral energy distribution (SED). A significant line from the IR spectrum is the rotational transition of CO due to its rich abundance in the disk and strong dipole moments. Hence CO has been known as an indicator to estimate the physical properties of the protoplanetary disk. Power-law fitting on the disk Intensity profile with CO lines is well matched in the intermediate region, but stiff inner edge of

the power-law profile does not reconcile. Thus, the previous theoretical model of the accretion disk (Lynden-Bell & Pringle 1974) had suggested an exponentially tapered profile. In this work, the simulation domain simply involves the surface density that scales as smoothed power-law function:

$$\Sigma(R) = \Sigma_0 \left(\frac{R^2 + R_{\rm s}^2}{R_{\rm s}^2} \right)^{-\frac{p}{2}}, \tag{2.1}$$

where R is mid-plane distance to the central star, $R_{\rm s}$ is softening radius suggested to avoid density cusp, and p is the order of surface density profile, which is suggested to be between 0.5 to 1 inferred from observations (Mundy et al. 1996; Lay, Carlstrom & Hills 1997; Wilner et al. 2000; Kitamura et al. 2002; Andrews & Williams 2007; Andrews et al. 2010).

2.2 Temperature

Except for external heating processes of companion stars and background radiation, the thermal evolution of the protoplanetary disk is governed by stellar radiation and viscous energy dissipation.

The host protostar intensely radiates as a blackbody. However due to high disk opacity in the vicinity of the protostar, the disk shields stellar radiation from directly penetrating through mid-plane. Thus the overall disk may only suffer the incident radiation into the disk through both disk surface sides. For a disk annulus in thermal equilibrium by absorbing stellar radiation of which flux decreases with distance as R^{-2} and radiatively cooling as a blackbody, approaching stellar radiation takes a reduction factor of $\cos\theta$ considering disk surface heating. Hence we may estimate the stellar luminosity on the disk surface scales as R^{-3}, so that

$$L_* \langle \cos\varphi \rangle \approx L_* \left(\frac{R_*}{R} \right) = \sigma T_*^4 = \frac{F_{\rm in}}{4\pi R^2} \left(\frac{R_*}{R} \right), \tag{2.2}$$

which yields the net incident flux $F_{\rm in}$

$$F_{\rm in} \propto \sigma T_*^4 \left(\frac{R}{R_*} \right)^{-3}. \tag{2.3}$$

The disk annulus in sequence re-radiates the incident stellar flux as a blackbody, then the emitting flux $F_{\rm em}$ becomes

$$F_{\rm em} \propto \sigma T_{\rm d}^4. \tag{2.4}$$

In thermal equilibrium, we can equate $F_{\rm in} = F_{\rm em}$ which results in disk temperature scaled as $R^{-3/4}$:

$$F_{\rm in} = F_{\rm em} \rightarrow T_{\rm d}(R) \propto T_* \left(\frac{R}{R_*} \right)^{-\frac{3}{4}}. \tag{2.5}$$

Mainly viscosity in the disk plays a role of angular momentum transport between the differential azimuthal velocities of the annuli. The relatively slow rotation of outer annulus drags the inner annulus so that the viscosity dissipates angular momentum, which continues the internal disk heating. If the viscous heating occurs in an annulus that lies over the disk from R to $R + \Delta R$ within the thermal timescale, the annulus is able to preserve the isothermal hydrostatic equilibrium by radiating a half of the gravitational potential through surface panels as a blackbody. Therefore the thermal equilibrium balanced with viscous energy dissipation and blackbody radiation is given by

$$\frac{GM_*\dot{M}}{2R}\frac{\Delta R}{R} \approx 2 \times 2\pi R\, \Delta R\, \sigma T_{\rm d}^4(R), \tag{2.6}$$

which is also written in disk temperature

$$T_{\rm d}(R) \approx \frac{GM_*\dot{M}}{8\pi\sigma R_*^3} \left(\frac{R}{R_*} \right)^{-\frac{3}{4}}, \tag{2.7}$$

where $\dot{M}$ is mass accretion rate of the annulus toward the central star. Although we have predicted the temperature profile from different two heating processes, both approaches correspond with the disk temperature that distributes as $R^{-3/4}$. However, the observation results of previous studies concluded that the disk temperature decreases as roughly $R^{-3/5}$ (the order of decrease varies in a range of 0.4-0.7 according to systems: 0.35-0.7 in T-Tauri and Herbig Ae/Be stars by Guilloteau & Dutrey 1998; Dutrey

& Guilloteau 2007; and 0.4-0.74 in samples of Ophiuchus-Scorpius star formation region by Andrews & Williams 2007). The disagreement signifies that the analytic argument describes a colder protoplanetary disk at the distant region than observation. One valid explanation is vertically flaring of the protoplanetary disk (Kenyon & Hartmann 1987). This supposition has been proved of edge-on Hubble images of the stellar object and its companion disk (e.g., Padgett et al. 1999), and can be verified by analysis of vertical disk structure in hydrostatic equilibrium. In accordance with the temperature profile, we introduce smoothed power-law function in this work:

$$T(R) = \left[T_{\rm s}^2 \left(\frac{R^2 + R_{\rm s}^2}{R_{\rm s}^2} \right)^{-q} + T_\infty^2 \right]^{\frac{1}{2}}, \tag{2.8}$$

in which $T_{\rm s}$ is scaling temperature at $R_{\rm s}$, and T_∞ means temperature at infinity far disk region.

Not mentioned the planet, but it radiates into its surroundings when accreting disk materials. The planet radiation does not threaten to disturb overall disk thermal properties but only overwhelms local temperature. Also, gravitational perturbation of planet mass in the disk forms an over-dense nonlinear structure like spiral arms that are obliged to heat the disk via gravitational torque. These heating processes of the planet may distort the morphology of the disk, which opens gaseous gaps and forms large unstable structures.

2.3 Density

In contrast that the surface density is estimated from an intensity profile, the veiled vertical structure of the disk does not allow us to know precise density profile. Rather than finding the exact density distribution, let us assume that the density can be written by a product of separable functions, so that

$$\rho(R, z) = \rho(R, 0) f(R, z), \tag{2.9}$$

where $\rho(R,0)$ is mid-plane density profile, and $f(R,z)$ is arbitrary dimension-less function which indicates vertical variation of the density. Integrating the density function along a vertical direction, we obtain the surface density

$$\Sigma(R) = \int_{-\bar{z}}^{\bar{z}} \rho(R,z)\,\mathrm{d}z = \int_{-\bar{z}}^{\bar{z}} \rho(R,0) f(R,z)\,\mathrm{d}z = \rho(R,0)F(R), \tag{2.10}$$

with conversion function between mid-plane density and surface density, which is defined as

$$F(R) = \int_{-\bar{z}}^{\bar{z}} f(R,z)\,\mathrm{d}z, \tag{2.11}$$

where $\bar{z}$ is a disk height at R. From the above relations, one derives the density profile written in terms of vertical distribution function $f(R,z)$ and surface density Σ(R):

$$\rho(R,z) = \frac{f(R,z)}{F(R)}\Sigma(R) = \Sigma_0 \frac{f(R,z)}{F(R)} \left(\frac{R_\mathrm{s}^2}{R^2+R_\mathrm{s}^2}\right)^{\frac{p}{2}}. \tag{2.12}$$

Although there is no direct way to determine vertical distribution function, we can here estimate the functional form in a specific case of the low-mass disk (i.e., $M_\mathrm{d} \ll M_*$). For a isothermal low-mass disk in hydrostatic equilibrium, the momentum equation in vertical direction is given by

$$\frac{\mathrm{d}P}{\mathrm{d}z} = c_\mathrm{s}^2 \frac{\mathrm{d}\rho}{\mathrm{d}z} = -\rho g_z = -\rho \frac{GM_* z}{(R^2+z^2)^{3/2}}, \tag{2.13}$$

which yields the gaussian vertical density profile as follow

$$\rho(z) = \rho_0 \exp(-z^2/2H^2), \tag{2.14}$$

and the scaled-height is defined as $H = c_\mathrm{s}/\Omega_\mathrm{K}$. Hence we suppose the initial density of the protoplanetary disk may vertically distribute as a quasi-gaussian function.

2.4 Vertical Structure

The hydrostatic equilibrium of the protoplanetary disk is balanced by gravitational potential of the disk and central star against thermal pressure and fluid flow. As previously alluded, fluid rotates around the central star with sub-Keplerian velocity, and

the potential can be calculated by considering the distribution of the host protostar and disk, whereas the pressure profile is unknown due to surface density and temperature profiles approximated as an intimate functional form. Thus it is a critical issue of the disk structure that how the thermal pressure exerts in the disk.

Despite uncertainty in disk thermal pressure, we plausibly believe that the pressure profile is characterized as a power-law function because both the surface density and temperature also do. Thus we suppose the power-law profile of thermal pressure given by

$$P(R,z) = P(z)\left(\frac{R}{R_0}\right)^{-\eta} \propto \rho(R,z)T(R,z), \tag{2.15}$$

where η is the order of the power-law distribution function in radial direction. Again the pressure profile cannot be found in the given information, but we may estimate the form with simple dimensional analysis. Since the pressure is proportional to a product of disk density and temperature, the radial pressure profile scales as

$$P(R,z_0) \sim \rho(R,z_0)T(R,z_0) \sim H^{-1}\Sigma(R)T(R) \sim R^{(3/2-p-q)} \sim R^{-\eta}, \tag{2.16}$$

where the scaled-height is considered that $H \sim \Omega_{\rm K}^{-1} \sim R^{-3/2}$, and thereby we have found $\eta = (p+q-3/2)$.

With the power-law pressure distribution, the disk in hydrostatic equilibrium yields the momentum equations of vertical and radial structures:

$$\frac{GM_*}{R^2}\frac{\bar{z}(R)}{R} + 2\pi G\Sigma(R) \approx k^2\frac{c_{\rm s}^2(R)}{\bar{z}(R)}, \tag{2.17}$$

$$\frac{GM_*}{R^2} - \eta\frac{c_{\rm s}^2}{R} \approx \frac{v_\phi^2}{R}, \tag{2.18}$$

of which vertical pressure gradient is calculated by

$$\frac{1}{\rho}\frac{\partial P}{\partial z}\bigg|_{z=\bar{z}} = -\left(\frac{\bar{z}}{H^2}\right)\frac{P}{\rho} \lesssim -k^2\frac{P/\rho}{\bar{z}(R)}, \tag{2.19}$$

where $c_{\rm s}$ is an isothermal sound speed, v_ϕ is an azimuthal gas velocity, and we define the coefficient $k = \max(\bar{z})/H < 1$. Here the radial momentum equation can be

written in azimuthal velocity

$$v_\phi = v_{\rm K}\left(1 - \eta\frac{c_{\rm s}^2}{v_{\rm K}^2}\right)^{\frac{1}{2}} \approx v_{\rm K}, \tag{2.20}$$

where $v_{\rm K} = (GM/R)^{1/2}$ is the Keplerian velocity. Commonly, the reduction from the Keplerian velocity is less than 1% and explained by the pressure gradient that offsets gravitational potential of the central star. Manipulating the momentum equation in vertical direction, we in turn obtain vertical structure of the protoplanetary disk as a function of mid-plane distance R:

$$\bar{z}(R) \approx \frac{\pi\Sigma(R)R^3}{2M_*} + \left[\left(\frac{\pi\Sigma(R)R^3}{2M_*}\right)^2 + \frac{k^2R^3}{GM_*}c_s^2\right]^{\frac{1}{2}}. \tag{2.21}$$

In initial simulation setup, we first relax the Keplerian disk and do fitting of the above functions to a distribution of the relaxed disk, from which one evaluates the coefficients again to construct more exact initial disk distribution.

Chapter 3

Dynamics

As we briefly referred to disk dynamics in the previous chapter, the hydrostatic disk structure is supported by the gravitational potential of the star and disk, thermal pressure, and fluid motion. However, the hydrostatic equilibrium no longer lasts but begins to falter due to internal processes.

Once gravitational instability takes place, the disk undergoes the dynamical evolution of planet formation, and the planet migrates by disk-planet interaction. During these disk-planet evolutions, the viscosity plays a critical role in dynamical evolution of the disk. Along with the gravitational torque, the viscosity is a primary mechanism for transports angular momentum transport in the accretion disk. Based on how efficient viscosity response is, accretion timescale in the circumplanetary disk is determined, which adjusts the growth rate of planet mass. As a result, the enhanced gravitational disk-planet interaction as much as mass growth accelerates the planet migration.

In order that the migrating planet sustains its hydrostatic atmosphere, the accretion should accompany extra energy release in the form of radiation, wind, or even jet. These feedbacks differ thermal evolution of the disk, which weakens over-dense structures such as spiral arms and circumplanetary disk, which may negatively interrupt planet growth via migration.

Not only viscosity, radiation, and disk-planet interaction, but the magnetic field is likely a crucial process in disk dynamics. Wardle (2007) argued that the disk is able to transport angular momentum by MHD turbulence or via the magneto-centrifugal acceleration of outflows from the disk surface, and the effective magneto-viscosity determines whether planets migrate inwards or outwards. However, the role of the magnetic field is still uncertain from which it loosely coupled with disk matters because the only disk surface is partially ionized due to stellar radiation. Furthermore, dust physics is never negligible in the aspect of observation and planet evolution. Dust population always give us clues of disk dynamics, and dust physics play a leading role in terrestrial planet formation and interior planet evolution (see, Nayakshin 2018).

Unfortunately, it is currently infeasible to achieve an ideal goal for numerical simulation reproducing the whole evolutionary history of the planetary system in the simulation domain with all kinds of multi-physics that can happen in the proplanetary disk. That requires extremely high computational cost, and there still have a problem in the numerical scheme to simulate multi-physics simultaneously. Nevertheless, in order to examine various phase of the planet migration with fundamental parameters, this work takes into account viscosity and radiation from the host protostar and the planet. In this chapter, we thus intend to deal with thermal and dynamical evolution of the disk, focusing on viscous process and radiative heating.

3.1 Viscosity

In order to understand how the viscosity operates in the protoplanetary disk, we have to understand which physical process generates the viscosity. The viscosity can be largely classified into two catalogs depending on whether the viscosity is caused by molecular interaction or turbulence. Thus the threshold for two viscosities is given by how the disk flow is turbulent. Evaluating the Reynolds number in the disk by adopting molecular hydrogen cross-section $\sigma_{\rm mole} \sim 10^{-15}\,{\rm cm}^2$, number density of

the disk $n \sim 10^{12}$ and scaling length $\Delta x \sim H \sim 10\,\mathrm{AU}$, we obtain

$$\mathrm{Re} \equiv \frac{UL}{\nu_{\mathrm{mole}}} = \frac{c_{\mathrm{s}}\Delta x}{\nu_{\mathrm{mole}}} = n\sigma_{\mathrm{mole}}\Delta x \approx 1.5 \times 10^{11} \gg 1. \tag{3.1}$$

This is a tremendous value that suggests the disk flow is turbulent without a doubt, but turbulent disk flow leads us to ask a subsequent question of 'what generates the turbulent flow?'. Unfortunately, the studies are underway to find the origin of the disk turbulence and its strength, but we merely presume that the turbulent motion can mainly occur by dust-gas interaction (Youdin 2005) or instability of magnetic fields (Lynden-Bell 1969; Balbus & Hawley 1991; Sano & Miyama 1999).

While the origin of the disk turbulent is not well understood, the magnitude of the turbulent viscosity is predictable via a dimensional analysis. Shakura & Sunyaev (1973) claimed that the turbulent viscosity is scaled with a product of the characterstic speed and length of the disk flow. Since the turbulent motion of the disk flow is vertically confined under the disk height and will rapidly decay in the nonlinear flow, parameters are limited in sound speed and scaled-height of the disk. Thus we write the parameterized Shakura & Sunyaev viscosity ν_{ss} that

$$\nu_{\mathrm{ss}} = \alpha_{\mathrm{ss}} c_{\mathrm{s}} H = \alpha_{\mathrm{ss}} \frac{c_{\mathrm{s}}^2}{\Omega_{\mathrm{K}}}, \tag{3.2}$$

in which α_{ss} is named Shakura-Sunyaev coefficient. In numerical studies, the α_{ss} is chosen in a range of $0.1 - 0.001$ according to the system, but one reliable candidate is $\alpha_{\mathrm{ss}} \approx 0.01$ of turbulence induced by magneto-rotational instability, which is a robust mechanism to generate turbulent motion in the disk (Forgan et al. 2010). In the numerical scheme of SPH method, however, it is inevitable to approximate the viscous flow by introducing artificial viscosity. The artificial viscosity generates nonlinear flow in the SPH simulation by dragging flows on purpose and relates to the Shakura & Sunyaev viscosity as

$$\alpha_{\mathrm{ss}} = \alpha_{\mathrm{sph}} \kappa \left(\frac{h_{\mathrm{sml}}}{2H} \right) = \alpha_{\mathrm{sph}} \kappa \left(\frac{c_{\mathrm{s}} h_{\mathrm{sml}}}{2\Omega_{\mathrm{K}}} \right), \tag{3.3}$$

where $h_{\rm sml}$ is the smoothing length, and κ is the order of unity that varies according to the kernel function (Cullen & Dehnen 2010). The smoothing length and scaled-height of the disk depends upon simulation resolution and disk mass, but the Shakura & Sunyaev viscosity becomes the order of one tenth of the artificial term in usual cases.

3.2 Thermal Evolution

For the accretion disk without stellar radiation, its thermal evolution is characterized by internal processes such as advective heat flow, viscous dissipation, and additional cooling/heating sources. Accordingly, the internal energy equation for the accretion disk is

$$\frac{\mathrm{d}u}{\mathrm{d}t} = \frac{\partial u}{\partial t} + \nabla \cdot (u\mathbf{v}) = -\frac{P}{\rho}\nabla \cdot \mathbf{v} + \Phi + \mathcal{L}, \tag{3.4}$$

where u is specific internal energy, $\mathcal{L}$ is heating/cooling source function, Φ is viscous dissipation which is given by

$$\Phi = \left(\frac{\partial u}{\partial t}\right)_{\nu} = \nu\left(R\frac{\partial \Omega_K}{\partial R}\right)^2 = \frac{9}{4}\nu\Omega_K^2, \tag{3.5}$$

and first divergence term indicates advective heat flow. This condition implies that the disk is inevitable to be thermally unstable when $\mathrm{d}u/\mathrm{d}t \neq 0$. Here we can realize that the disk essentially requires the cooling source function (i.e., $\mathcal{L} < 0$) for the accretion disk to be in thermal equilibrium.

By considering gas flow in the accretion disk, which is practically rotating with Keplerian velocity and steadily moves inward with δv due to the viscosity

$$v_{\rm g} = v_r\,\hat{\mathbf{e}}_r + v_\phi\,\hat{\mathbf{e}}_\phi + v_z\,\hat{\mathbf{e}}_z \approx -\delta v\,\hat{\mathbf{e}}_r + v_{\rm K}\,\hat{\mathbf{e}}_\phi, \tag{3.6}$$

its corresponding divergence becomes

$$\nabla \cdot \mathbf{v} = \frac{1}{r}\frac{\partial r v_r}{\partial r} + \frac{1}{r}\frac{\partial v_\phi}{\partial \phi} = -\frac{\delta v}{r} \approx 0 \tag{3.7}$$

because of negligible infall rate (i.e., $\delta v \ll 1$). Hence thermal evolution of the accretion disk is governed by viscous energy dissipation and source function:

$$\frac{\mathrm{d}u}{\mathrm{d}t} \approx \Phi + \mathcal{L}. \tag{3.8}$$

Therefore for the thermal equilibrium of the proplanetary disk, an internal cooling mechanism should compensate the heating via viscous dissipation (i.e., $|\mathcal{L}| \approx |\Phi|$).

3.2.1 Beta-cooling Model

Now we understand that the protoplanetary disk is intrinsically turbulent and that an underlying cooling mechanism in the disk is necessary for the thermal equilibrium. The proper mechanism of cooling is disk self-radiation, however, it is difficult to come up with a specific physical process that cools down as a function of Keplerian frequency (i.e., $\mathcal{L} \propto \Omega_{\mathrm{K}}^2$). People sketchy expect that collection of ices, molecules, and dust act as a coolant, but the chemical composition and distribution of the protoplanetary disk is still behind understanding (e.g., the chemical composition of the protoplanetary disk is previously studied in Pollack et al. 1994; Henning & Stognienko 1996; Bell et al. 1997; Semenov 2003).

To simplify the cooling mechanism, we again try to introduce parameterized cooling function which is radiatively cooling the disk within the cooling timescale. From the Shakura-Sunyaev α prescription, we obtain viscous dissipation as a function of Keplerian frequency, so that

$$\left(\frac{\partial u}{\partial t}\right)_{\nu} = \Phi = \frac{9}{4}\nu\Omega_{\mathrm{K}}^2 = \frac{9}{4}\alpha_{\mathrm{ss}}c_{\mathrm{s}}^2\Omega_{\mathrm{K}} \sim \Omega_{\mathrm{K}}, \tag{3.9}$$

and its corresponding viscous heating timescale approximates

$$t_{\mathrm{heat}} \approx \frac{u}{(\partial u/\partial t)_{\nu}} = \frac{u}{\Phi} = \frac{4}{9\alpha_{\mathrm{ss}}\gamma(\gamma-1)}\Omega_K^{-1} \tag{3.10}$$

that is proportional to local dynamical timescale (i.e., $t_{\mathrm{heat}} \propto \Omega_K^{-1}$). In this aspect, we plausibly estimate a cooling timescale comparable to heating timescale as

$$t_{\mathrm{cool}} = \beta\Omega_{\mathrm{K}}^{-1}, \tag{3.11}$$

which yields a parameterized cooling rate

$$\mathcal{L} = \left(\frac{\partial u}{\partial t}\right)_{\rm cool} \approx -\frac{u}{t_{\rm cool}} = -\frac{u\Omega_{\rm K}}{\beta}, \tag{3.12}$$

where β is an arbitrary constant that determines the cooling rate. This β-cooling model is first suggested by Gammie (2001) to study disk condition for gravitational instability of gas giant formation. In his work, the instability happens when $\beta = 3$ with specific heat ratio $\gamma = 2$. In conclusion, we have employed two parameters of Shakura-Sunyaev α viscosity and β coefficient to understand the thermal evolution of the protoplanetary disk. The two parameters seem independent each other, but the thermal equilibrium of the disk requires a pair of comparable cooling and heating timescale. We therefore write the relation

$$\frac{4}{9\alpha_{\rm ss}\gamma(\gamma-1)} = \beta. \tag{3.13}$$

Taking $\alpha_{\rm ss} = 0.01$, and $\gamma = 1.4$ for diatomic components, we estimate that $\beta \approx 80$. The estimated large β implies a slow cooling rate but may be stimulated with rapid accretion flow into the central star (i.e., $|\nabla \cdot \mathbf{v}| \gg 1$) or by including stellar radiation (i.e., $\mathcal{L} = \mathcal{L}_{\rm beta} + \mathcal{L}_{\rm radi}$).

3.2.2 Stellar and Planet Radiation

So far we did not include the effect of stellar radiation when accounting for the thermal equilibrium of the disk. However, the role of the protostar of which strong radiation ranges from FUV to X-rays is crucial in the thermal process of the disk. The previous study loosely concluded that the photoevaporation of the stellar radiation disperses the matters of disk surface as outflow, of which mass loss will affect the dynamical evolution of the disk. For the innermost region of a stellar magnetosphere where the stellar magnetic field is intense enough to disturb the disk structure by accreting disk materials along its field lines and by providing accretion feedback, the planet migration is likely to be halted by coupling of stellar magnetic field and planet (Armitage 2015).

This work for simplification assume the disk distributes beyond the stellar magnetosphere, and the mass loss rate of outflow driven by photoevaporation is comparably negligible within the period of planet migration. Then underlying stellar radiation in overall the disk is estimated by

$$T_{\mathrm{irr},*}(R) = T_* \left(\frac{R}{R_\mathrm{s}} \right)^{-q}. \tag{3.14}$$

This assumption is valid for the thermal equilibrium of disk because the stellar radiative heating follows the initial temperature profile scaled with R^{-q}.

The planet luminosity can be described in the planet irradiation with its effective temperature ($L_\mathrm{eff} \sim T_\mathrm{eff}^4$) and accretion feedback ($L_\mathrm{feed} \sim \dot{M}_\mathrm{p}$), but we understand that the effective temperature is not sufficient to generate significant radiative heating for the surroundings (Nayakshin 2014). Note that negligible planet irradiation (i.e., $L_\mathrm{p} \approx L_\mathrm{feed}$), we formalize accretion feedback of the planet as much as its accreting energy of the disk materials, so that

$$L_\mathrm{p} \approx \frac{G M_\mathrm{p} \dot{M}_\mathrm{p}}{R_\mathrm{feed}} = 4\pi |\mathbf{r} - \mathbf{r}_\mathrm{p}|^2 \sigma T_{\mathrm{irr,p}}^4, \tag{3.15}$$

where $|\mathbf{r} - \mathbf{r}_\mathrm{p}|$ is a distance to the planet, and R_feed is a feedback radius that regulates the strength of radiative feedback. The regular size of the feedback radius is obscure (ranging $1 - 10\, R_\odot$) but is evaluated by both fraction of accreted energy converted into radiation and boundary of the hydrostatic atmosphere of the planet in which the planet exchange mass and energy to the disk (Stamatellos 2017). Considering geometric reduction on the planet radiation which can be radiated away through disk surface due to high opacity of the disk, we roughly calculate the amount of planet luminosity that incidents on the disk surface as $1/4\, L_\mathrm{p}$. As a result, radiative temperature of the planet becomes

$$T_{\mathrm{irr,p}}(\mathbf{r}) = \left(\frac{L_p}{16\pi\sigma |\mathbf{r} - \mathbf{r}_p|^2} \right)^{\frac{1}{4}} = \left(\frac{G M_\mathrm{p} \dot{M}_\mathrm{p} / R_\mathrm{feed}}{16\pi\sigma |\mathbf{r} - \mathbf{r}_p|^2} \right)^{\frac{1}{4}} \tag{3.16}$$

Back to the thermal evolution of the accretion disk, let us modify β-cooling model with radiative heating of the star and planet. Applying radiative processes, we define

the effective internal energy u_{eff} that represents the collective effect of radiation and β-cooling as $u_{\rm eff} = (u - u_{\rm irr,*} - u_{\rm irr,p})$, where $u_{\rm irr,*}$ and $u_{\rm irr,p}$ are increase of internal energy due to stellar and planet radiation respectively. With the effective internal energy, one provides effective β-cooling rate:

$$\left(\frac{\partial u}{\partial t}\right)_{\rm cool} \approx \frac{u_{\rm eff}}{t_{\rm cool}} = -\frac{(u - u_{\rm irr,*} - u_{\rm irr,acc})}{t_{\rm cool}} = -\frac{(u - u_{\rm irr,*} - u_{\rm irr,p})\Omega_{\rm K}}{\beta}. \quad (3.17)$$

Note that the β-cooling is paradoxically able to operate heating process in which $u_{\rm eff} < 0$. Therefore the governing equation of disk thermal evolution with β-cooling model becomes

$$\frac{{\rm d}u}{{\rm d}t} = \frac{\partial u}{\partial t} + \nabla \cdot (u\mathbf{v}) = -\frac{P}{\rho}\nabla \cdot \mathbf{v} + \frac{9}{4}\nu\Omega_K^2 - \frac{(u - u_{\rm irr,*} - u_{\rm irr,p})\Omega_{\rm K}}{\beta}. \quad (3.18)$$

Chapter 4

Numerical Algorithms

In this chapter, we depict numerical scheme for accretion and thermal evolution in the GIZMO. As we alluded the important role of accretion and thermal evolution in the planet migration, the numerical method of them demands efficient performance and accurate calculation to investigate the dynamical evolution of the planet in the protoplanetary disk. Hence this work has expanded GIZMO with optimized accretion method and β-cooling model. The numerical algorithms of them are going to be described in the below sections.

4.1 Accretion Scheme

In the simulation domain, the seed particles (e.g., star and planet) accretes gaseous particles in the following: The code first searches active particles entered into the interaction sphere from Tree-Particle-Mesh and verifies physical quantities whether they are potential to be accreted. With the list of the accretion particles, the code also evaluates averaged accretion timescale for the mass growth rate. Then from the accretion flow and its corresponding timescale, the conservative physical quantities are calculated to update kinematics of the seed particle. Thereafter, the accreted particles are annihilated from the domain. Let us now introduce the detail processes of the accre-

tion scheme.

4.1.1 Accretion Criteria

By astrophysical definition, the accretion designates a situation that massive compact body (e.g., star, and planet) accumulates surrounding matters by gravitational attraction. However, note that the gravitational interaction does not always lead to accretion. The surrounding matters will escape the interaction zone if they are not bound under the gravitational potential of the primary object. Furthermore, the gravitationally bound materials may keep the orbital motion with its sufficient relative angular momentum. Satisfying all accretion conditions in practice, the materials falling onto the object eventually arrive at a boundary in which the primary object accretes the mass and provides feedback into the surroundings.

In order that the simulation domain reproduces the accretion process, we first need to define accretion radius $R_{\rm acc}$ which is an artificial distance designed to solve the resolution problem of the simulation. In the astrophysical situation of the accretion disk, the hydrostatic atmosphere of the primary object continues to the accretion disk, or the magnetized object channels the accretion flow onto its hot-spot along the magnetic field. Hence, unless the magnetic strength is extremely high to widely separate the accretion region from the object, it is difficult to resolve the accretion flow in the simulation domain. Therefore, the numerical algorithm agrees with treatment that the accretion is considered to annihilate particles within the accretion radius comparable with simulation resolution.

For the protoplanetary disk, we define the accretion radius to be less than 'Hill-radius' which is given by

$$R_{\rm H} = \alpha \left(\frac{M_{\rm p}}{3M_*} \right)^{\frac{1}{3}} \gg R_{\rm acc}, \tag{4.1}$$

where α is an orbital separation of the planet. Taking Jupiter mass of the plant hosted by solar mass star and orbital separation of $100\,{\rm AU}$, the Hill radius becomes $R_{\rm H} \approx$

7 AU. Here we note that the gravitational attraction of the planet exceeds the stellar influence within the Hill-radius. Here we note that the gravitational attraction of the planet exceeds the stellar influence within the Hill-radius. The disk materials that invade the Hill-sphere are going to form the circumplanetary disk rotating around the planet with sub-Keplerian velocities and gradually spiral inward by internal processes. Thereby the planet accretion may occur when the disk materials enough approach to the planet within a few fractions of the Hill-radius. Therefore, we define the accretion radius with fractional term f, so that

$$R_{\rm acc} = f\alpha\left(\frac{M_{\rm p}}{3M_*}\right)^{\frac{1}{3}}. \tag{4.2}$$

If the accretion radius is over-estimated (i.e., $f \approx 1$), the accretion rate may be over-estimated since the migration timescale of the disk material within the accretion sphere can take longer time than simulation time step. To avoid inaccurate accretion flow, we reduce the accretion radius until it is analogous with smoothing length (i.e., $R_{\rm acc} \gtrsim h_{\rm sml}$) which is the limited resolution of the particle-based method. In this work, we find a valid fraction of $f = 0.05$. Along with the accretion radius, the accretion scheme sequentially verifies three accretion criteria to create the list of accreted gaseous particles and calculate the accretion flow.

The following accretion scheme has modified the algorithm of Hubber (2012) to be suitable in the GIZMO. At the first criterion, all the gaseous particles involved within the accretion sphere of the seed particle are marked as the candidate:

$$\Delta\mathbf{r} = |\mathbf{r} - \mathbf{r}_{\rm p}| < R_{\rm acc} + h_{\rm sml}. \tag{4.3}$$

The additional term of the smoothing length considers extended gaseous particles smoothed by the kernel function $W(\mathbf{r}, h)$. Although the gaseous particle beyond the accretion sphere is ruled out from the accretion flow, it can be partially included by overlapping with kernel area. Hence we also include the gaseous particles that span the boundary.

Among the particles within the accretion disk, we evaluate the relative energy between the seed and gaseous particles and select gravitationally bound particles of which relative energy is negative, as the second criterion. The total relative energy between the seed and gaseous particle becomes

$$e = \frac{1}{2}\mu|\Delta\mathbf{v}|^2 + \frac{G\mu\bar{M}}{2}\left[\phi\left(\frac{|\Delta\mathbf{r}|}{h}\right) + \phi\left(\frac{|\Delta\mathbf{r}|}{R_{\rm acc}}\right)\right], \tag{4.4}$$

where μ and $\bar{M}$ are reduced mass, and $\phi(\mathbf{r}, h)$ is the potential kernel function which is calculated by

$$\begin{aligned}\phi(\mathbf{r}, h) = 4\pi\Bigg(&- \frac{1}{r}\int_0^r W(\mathbf{r}', h)\, r'^2\, \mathrm{d}r' \\ &+ \int_0^r W(\mathbf{r}', h)\, r'\, \mathrm{d}r' - \int_0^{2h} W(\mathbf{r}', h)\, r'\, \mathrm{d}r'\Bigg).\end{aligned} \tag{4.5}$$

For example, potential kernel for cubic spline kernel function with $s = r/h$ is given by

$$\phi(\mathbf{r}, h)_{\rm cubic} = \begin{cases} \frac{14}{5} - s^2\left[\frac{16}{3} + s^2\left(\frac{32}{5}s - \frac{48}{5}\right)\right], & (0 < s < 0.5) \\ \frac{16}{5} - \frac{1}{15s} + s^2\left[\frac{32}{3} - s\left\{16 - s\left(\frac{48}{5} - \frac{31}{15}s\right)\right\}\right], & (0.5 < s < 1) \\ \frac{1}{s}, & (s > 1) \end{cases} \tag{4.6}$$

Except for the gaseous particle has negative total relative energy, the accretion scheme filters escaping particles.

The gravitationally bound particles now intend to keep orbital motion around the seed or fall into the seed in accretion timescale. For the particles to be accreted, they should exhibit relative angular momentum less than Keplerian angular momentum at the boundary:

$$|\Delta\mathbf{r} \times \Delta\mathbf{v}| < (GM_{\rm p}R_{\rm acc})^{\frac{1}{2}}. \tag{4.7}$$

We here may anticipate that the third criterion in the planet migration has marginal importance because the particle already spirals from the circumplanetary disk into the accretion sphere by losing angular momentum via gravitational torque and viscosity.

4.1.2 Accretion Timescale

While the accretion criteria quantitatively judge the accretion flow, its corresponding time scale is vague as we set an artificial accretion radius. Nonetheless, the accretion time scale determines the accretion rate of the disk materials, which estimate the strength of the accretion feedback (e.g., $L_{\rm p} \sim \dot{M}_{\rm p}$). In the numerical treatment, we estimate the accretion rate considered in two types of accretion flow with the kernel-averaged term of the accretion particles (Hubber 2012).

For the spherical accretion flow that converges onto the seed particle, the mass accretion rate is described in

$$\dot{M}_{\rm infall} = -4\pi|\Delta\mathbf{r}|\Delta\mathbf{r}\cdot\Delta\mathbf{v}\rho_{\rm acc}, \tag{4.8}$$

with density of accretion particles $\rho_{\rm acc}$. Applying kernel-weighted term on the individual accretion particles, we evaluate kernel-averaged accretion time scale for infall accretion as

$$\langle t_{\rm infall}\rangle = \frac{\sum_j m_j\mathcal{W}}{4\pi\sum_j|\Delta\mathbf{r}_{js}|\Delta\mathbf{r}_{js}\cdot\Delta\mathbf{v}_{js}m_j\mathcal{W}}, \tag{4.9}$$

in which subscripts j and s indicate the individual gaseous and seed particle respectively, and the weight sum is defined by

$$\mathcal{W} = \Sigma_j m_j W(\mathbf{r}_{js}, H_{\rm acc})/\rho_j. \tag{4.10}$$

Another possible scenario of the accretion flow is the gaseous particles steadily spiral around the seed particle by losing angular momentum via viscous dissipation. Using the Shakura-Sunyaev α prescription again, the viscous accretion timescale is roughly given by

$$t_{\rm vis} \approx \frac{(\Delta r)^2}{\nu_{\rm ss}} = \frac{\Omega'_{\rm K}(\Delta r)^2}{\alpha_{\rm ss}c_{\rm s}^2} \tag{4.11}$$

with local angular frequency $\Omega'_{\rm K}$, and then one also yields kernel-averaged viscous accretion timescale:

$$\langle t_{\rm vis}\rangle = \frac{(GM_s)^{1/2}}{\alpha_{\rm ss}\mathcal{W}}\sum_j\frac{|\Delta\mathbf{r}_{js}|^{1/2}m_j\mathcal{W}}{\rho_j c_{{\rm s},j}^2}. \tag{4.12}$$

Combining the above accretion timescales, we conclude the artificial accretion timescale in terms of the weighted fractions determined by the accretion flow, so that

$$t_{\rm acc} = \langle t_{\rm infall} \rangle^{(1-f)} \langle t_{\rm vis} \rangle^{f}, \tag{4.13}$$

where f is weighting power chosen by

$$f = \min\left[\frac{2\langle E_{\rm kin}\rangle}{\langle E_{\rm grav}\rangle}, 1\right], \tag{4.14}$$

with the kinetic $E_{\rm kin}$ and gravitational $E_{\rm grav}$ energies of the accretion flow. We estimate the relative energies in

$$E_{\rm rot} = \frac{1}{2}\frac{\Sigma_j (m_j |\Delta\mathbf{r}_{js} \times \Delta\mathbf{L}_{js}|)^2}{\Sigma_j m |\Delta\mathbf{r}_{js}|^2}, \tag{4.15}$$

$$\begin{aligned} E_{\rm grav} = {} & \frac{GM_s}{2}\sum_j m_j [\phi(\Delta\mathbf{r}_{js}, h_j) + \phi(\Delta\mathbf{r}_{js}, R_{\rm acc})] \\ & + \frac{G}{4}\sum_j \sum_{j' \neq j} m_j m_{j'} [\phi(\Delta\mathbf{r}_{js}, h_j) + \phi(\Delta\mathbf{r}_{j's}, h_{j'})]. \end{aligned} \tag{4.16}$$

In the numerical simulation of the planet accretion, we find that the f is asymptotically the unity, which means the circumplanetary disk transports angular momentum outward dominantly by the viscous dissipation.

4.1.3 Conservative Quantities

After the accretion scheme finishes searching the particles that satisfy the accretion criteria and calculating the accretion rate, the accreted particles are annihilated by transporting their physical quantities to the seed particle. Under the conservation laws,

the physical quantities of the seed planet are updated as follows

$$M_s' = M_s + \sum_j \delta m_j, \tag{4.17}$$

$$\mathbf{r}_s' = M_s'^{-1}\left(M_s\mathbf{r}_s + \sum_j \delta m_j \mathbf{r}_j\right), \tag{4.18}$$

$$\mathbf{v}_s' = M_s'^{-1}\left(M_s\mathbf{v}_s + \sum_j \delta m_j \mathbf{v}_j\right), \tag{4.19}$$

$$\mathbf{L}_s' = \mathbf{L}_s + \sum_j \delta m_j \Delta\mathbf{r}_{js} \times \Delta\mathbf{v}_{js} \tag{4.20}$$

in which $\mathbf{L}_\mathrm{s}$ means spin angular momentum of the seed particle, and δm_j is mass reduction of the gaseous particle.

The accretion timescale normally exceeds the its simulation time step Δt_j, then the increase of the seed mass without delay may cause an over-estimated accretion rate. Therefore, we adopt the retarded mass growth along the simulation time step, so that

$$\delta m_j = m_j\left[1 - \exp\left(-\frac{\Delta t_j}{t_\mathrm{acc}}\right)\right]. \tag{4.21}$$

The remaining mass gradually dissipates over the simulation time. Otherwise, when the accretion especially is shorter than the simulation time step, We substitute the numerical time step into accretion timescale and immediately eliminate the gaseous particle from the simulation domain by (i.e., $\delta m_j = m_j$). At the end of the update of physical quantities, the accretion scheme approximate the accretion rate in

$$\dot{M}_s = \frac{\mathrm{d}M_s}{\mathrm{d}t} \approx \frac{\sum_j \delta m_j}{t_\mathrm{acc}}. \tag{4.22}$$

4.2 Update of Thermal Evolution

Once the accretion scheme finished updating kinematics of the seed and evaluating accretion rate, the code in turn is prepared to calculate energy generation rates with β-cooling model. Here the scheme for thermal evolution should be compatible with

the integration scheme. In the GIZMO code, the position and velocity are numerically integrated by kick-drift-kick leapfrog scheme in sequence

$$\mathbf{v}^{n+1/2} = \mathbf{v}^{n} + \mathbf{a}^{n}(\Delta t/2), \tag{4.23}$$

$$\mathbf{r}^{n+1} = \mathbf{r}^{n} + \mathbf{v}^{n+1/2}\Delta t, \tag{4.24}$$

$$\mathbf{v}^{n+1} = \mathbf{v}^{n+1/2} + \mathbf{a}^{n+1/2}(\Delta t/2), \tag{4.25}$$

of which positions and velocities are alternately updating for every half numerical timescale, Δt is a numerical time step. Since the gravity and hydrodynamics to be updated require both positions and velocities, they should be updated at $n+1/2$-th time step. Whereas we update the β-cooling function in full time step because the functions of β-cooling model depends on the distance between seed and particle. Therefore, the internal energy of β-cooling model in the kick-drift-kick leapfrog scheme is renewed by

$$u^{n+1/2} = u^{n} + \Delta u^{n}_{\rm hydro} + \Delta u^{n}_{\rm gravity}, \tag{4.26}$$

$$u^{*} = u^{n+1/2} + \Delta u^{n+1/2}_{\rm hydro} + \Delta u^{n+1/2}_{\rm gravity}, \tag{4.27}$$

$$u^{n+1} = u^{*} + \Delta u^{n}_{\rm beta}, \tag{4.28}$$

where the radiative energy change by the β-cooling $\Delta u_{\rm beta}$ is given by

$$\Delta u^{n}_{\rm beta} = (\partial u/\partial t)_{\rm cool}\Delta t = -(u^{*} - u_{\rm irr,*} - u_{\rm irr,p})(\Omega_K/\beta)\Delta t. \tag{4.29}$$

Chapter 5

Simulations

We implement the numerical simulation of the planet migration with the disk thermal evolution and the accretion method. Prior to the simulation of the planet migration, we have examined Bondi-accretion test to verify the accuracy of accretion scheme established in the GIZMO and found the test results in reliable numerical value comparable with an analytic solution within a few percentages of difference. With validity on our accretion method, we have simulated a total of twenty models in wide parameter space varying initial mass and orbital radius of the planet, β coefficient, and strength of planet radiative feedback. The numerical methodology and simulation results are introduced in the below sections.

5.1 Bondi Accretion Test

In this section, we perform Bondi-Ebert spherical accretion test in order to confirm whether the accretion method in the GIZMO accurately calculates accretion rate. To compare the numerical performance of this work, we reproduced an identical problem tested by Hubber (2012) who measured the accretion rate with different accretion radii. By solving the Bernoulli equation, the transonic Bondi-accretion rate for an isothermal

medium is given by

$$\dot{M}_{\rm acc} = \frac{e^{3/2}\pi G^2 M_s^2 \rho_\infty}{c_{\rm iso}^3}, \tag{5.1}$$

where $c_{\rm iso} = (P/\rho)^{1/2}$ is an isothermal sound speed and ρ_∞ represents density at infinite far region. At the outside of sonic radius $R_{\rm sonic}$,

$$R_{\rm sonic} = \frac{R_{\rm B}}{2} = \frac{GM_s}{2c_{\rm iso}^2}, \tag{5.2}$$

the subsonic inflow is derived by the pressure gradient, but the accretion rate reaches the sound speed at the sonic radius and freely falls into the central object by gravitational attraction. Note that the Bondi-accretion rate is calculated by neglecting self-gravity of the medium.

5.1.1 Initial Simulation Setup

The test domain uses adiabatic heat ratio as $\gamma = 1.01$ to deal with an isothermal medium and assumes the unity of mean molecular weight for simple calculation. The simulation domain initially includes 5×10^5 medium particles, and each particle is assigned with identical mass and specific internal energy. To set $R_{\rm sonic} = 1$, we adequately choose mass and specific internal energy and take the sonic radius as the simulation unit. Accordingly, the domain is set to be a periodic box of 100×100 size.

We relax the isothermal medium in the simulation domain in order to obtain uniform density distribution until the density fluctuation becomes less than $1\,\%$. From the relaxed medium, we sample the particles within $50\,R_{\rm sonic}$ (consequently, the simulation domain leaves 2.5×10^5 particles) and place a central object that always maintains its position. In the Bondi-accretion test, the accretion scheme does not increase the mass of the central object and only counts the accretion rate, and an analytic function gives the gravitational potential in the form of GM/r^2 (without taking into account self-gravity of the medium)

5.1.2 Bondi-accretion Rate

We perform five models with different accretion radii $R_{\rm acc} = 0.5$, 1, 2, 4, and 8 $R_{\rm sonic}$, using retarded accretion scheme which prevents over-estimating the accretion rate within the simulation timescale. The simulations implement for $t_{\rm sim} = GM_s/c_{\rm iso}^3$ which is much longer period compared with dynamical timescale of Bondi-accretion (i.e., $t_{\rm ff} \approx GM/2\sqrt{2}c_{\rm iso}^3$). Thus we are convinced that the accretion flow fully achieves steady inflow at the end of the simulation. We also reproduce models with the immediate accretion scheme for the comparison. In the **Figure 5.1**, we plot the relative

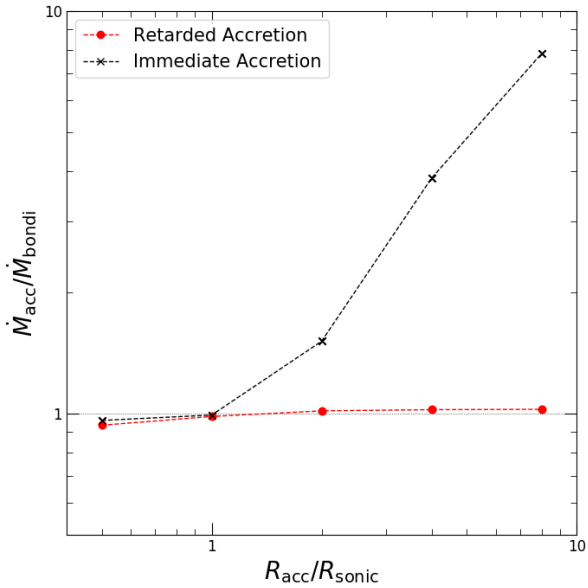

Figure 5.1: Relative Bondi-accretion rate as a function of accretion radius: Each markers indicates individual simulations and are connected by dashed line. The retarded accretion scheme is colored by red, and the immediate accretion scheme is black.

accretion rate as a function of the accretion radius. At $R_{\rm acc} < R_{\rm sonic}$, both accretion schemes result in slightly under-estimated accretion rate (within a few percentages) compared to the analytical solution. When the accretion radius is set to be larger than

the sonic radius, the immediate accretion scheme largely over-estimates the accretion rate as the accretion radius lengthens, while the accretion rate estimated by the retarded accretion scheme exceeds the analytic expectation less than one percent. The significant over-estimation in the immediate accretion scheme is thought to be caused by an artificial pressure gradient due to the sudden annihilation of particles (Hubber 2012).

We confirm the validity of the retarded accretion scheme in the GIZMO by reproducing the Bondi-accretion test of Hubber 2012. According to the results of Bondi-accretion test, we understand both accretion schemes calculate a relatively accurate accretion rate within negligible difference if the scheme takes an infinitesimal size of the accretion radius. In the planet migration, both accretion schemes thus are likely to yield relatively comparable accretion rates of the planet with the accretion radius that is set to be a few fractions of the Hill radius (i.e., $R_{\rm acc} = 0.05 R_{\rm Hill}$). However, applying the retarded accretion scheme is essential to deal with interaction between the disk and planet accurately because a slight change in accretion rate can largely alter the mass growth of the planet and the strength of radiative feedback, allowing different migration process of the planet.

5.2 Planet Migrations with GIZMO

To investigate the planet migration that depends on initial physical quantities of the planet and internal processes of the disk, we set following crucial parameter spaces:

(a) Initial orbital separation of the planet: $\alpha_{\rm init} = 30, 50, 60, 80\,{\rm AU}$

(b) Initial planet mass: $M_{\rm p,init} = 0.5, 2, 5\,M_{\rm J}$

(c) Radiative cooling rate: $\beta = 1, 3, 10$

(d) Feedback radius of the planet radiation: $R_{\rm feed} = 1, 5, 10, 20\,R_{\odot}$

A standard model of this work involves the planet with $M_{\rm p} = 2\,M_{\rm J}$ that initially locates at $\alpha_{\rm init} = 60\,{\rm AU}$ from the central star and radiates accreted energy away with

$R_{\rm feed} = 1\,R_\odot$ in the disk. In order to characterize internal processes of the disk, we prescribe Shakura-Sunyaev viscosity with $\alpha_{\rm ss} = 0.01$ and β-cooling model with $\beta = 3$ which is threshold value for planet formation via gravitational instability in GIZMO (Deng et al. 2017). Varying parameters in the standard model, we establish twenty numerical models listed in **Table 7.1-3**. Considering evolutionary timescale for planet migration, we let the disk evolve in the simulation domain for 10,000 years which is ten orbital periods of the outmost disk region.

5.2.1 Numerical Methodologies

Initial Setup for Protoplanetary Disk

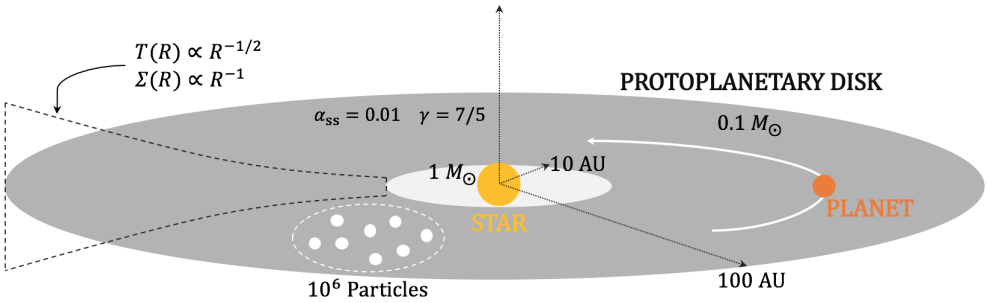

Figure 5.2: Schematic illustration of protoplanetary disk in the simulation domain: The central star with $M_* = 1\,M_\odot$ hosts the protoplanetary disk with $M_{\rm d} = 0.1\,M_\odot$ that features the surface density $\Sigma(R) \propto R^{-1}$ and temperature profile $T(R) \propto R^{-1/2}$. We set the disk initially distributes from $10 - 100\,{\rm AU}$ and consists of diatomic molecules (i.e., $\gamma = 7/5$). Disk viscosity is prescribed with Shakura & Sunyaev (1964) α viscosity with $\alpha_{\rm ss} = 0.01$.

We commonly use a massive protoplanetary disk with $M_{\rm d} = 0.1\,M_\odot$ hosted by the central star of $M_* = 1\,M_\odot$. The disk is described with one million gaseous particles and initially distributes from 10 to 100 AU. For agreement with observation, we choose

the surface density and temperature profiles with $p = 1$ and $q = 0.5$ respectively,

$$\Sigma(R) = \Sigma_0 \left(\frac{R^2 + R_{\rm s}^2}{R_{\rm s}^2} \right)^{-\frac{1}{2}}, \tag{5.3}$$

$$T(R) = \left[T_{\rm s}^2 \left(\frac{R^2 + R_{\rm s}^2}{R_{\rm s}^2} \right)^{-\frac{1}{2}} + T_\infty^2 \right]^{\frac{1}{2}}, \tag{5.4}$$

with $R_{\rm s} = 1\,{\rm AU}$ and $T_\infty = 20\,{\rm K}$. In the simulation domain, the gaseous particles randomly distributes in the disk structure by following the profiles of surface and vertical density. Each particles initially rotates with Keplerian velocity and exhibits specific internal energy corresponding to temperature profile without considering vertical distribution. These initial setup makes the disk structure not satisfy hydrostatic equilibrium, so the stiff pressure gradient at the disk boundary vastly expands the disk. The disk expansion gradually establishes an equilibrium by balancing with thermal pressure and gravitational potential. For the disk to be fully relaxed, we previously implement the disk relaxation for ten orbital periods of the outmost disk region. The overall relaxed disk structure sustains its initial temperature profile, but the temperature rises by viscous heating as approaching the dense central region. The dominant viscosity at the central region also induces accretion flow into the star by dissipating disk angular momentum then trims the central surface density. As the disk material is accreted onto the star by losing its angular momentum, we witness the relaxed disk forming ring structures at the central region to conserve disk angular momentum. The artificial boundaries of the initial disk structure separated by surface density profile smooth through the relaxation.

With the relaxed disk, we set the planet that circularly orbits with Keplerian velocity according to its orbital separation. The accretion radius of the central star is fixed at $R_{\rm acc,*} = 1\,{\rm AU}$, whereas the planet accretes gaseous particles within $R_{\rm acc,p} = 0.05(M_{\rm p}/3M_*)^{1/3}$.

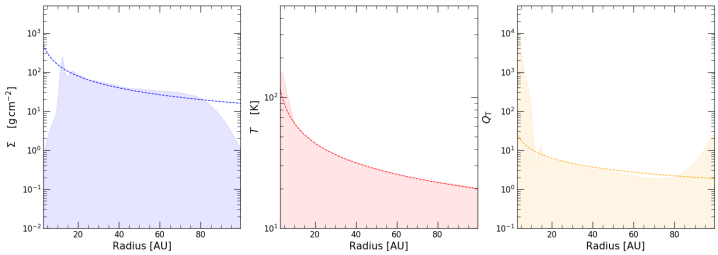

Figure 5.3: Initial disk thermal properties after dynamical relaxation: [LEFT] surface density, [MIDDLE] temperature, [RIGHT] Toomre $Q_{\rm T}$ parameter. The dashed lines indicates initial profiles given by simulation setup

Treatment of Disk Thermal Evolution

As alluded in the chapter of the disk dynamics, we introduce idealized β-cooling model and parameterized radiative heating of star and planet for disk thermal evolution. Since stellar radiation underlies disk temperature, we consider the heating of stellar radiation should yield a similar temperature profile of the initial disk structure. So we simply deal with the effect of stellar radiative heating as following temperature function

$$T_{\rm irr,*}(R) = T_*\left(\frac{R}{R_{\rm s}}\right)^{-\frac{1}{2}}, \tag{5.5}$$

The heating by the planet radiative feedback is taken into account with the accretion rate, and its corresponding heating temperature is given by

$$T_{\rm irr,p}(r) = \left(\frac{L_p}{16\pi\sigma|\mathbf{r}-\mathbf{r}_p|^2}\right)^{\frac{1}{4}}, \tag{5.6}$$

where we estimate the planet luminosity as

$$L_{\rm p} = \frac{GM_{\rm p}\dot{M}_{\rm p}}{R_{\rm feed}}. \tag{5.7}$$

Applying radiative heating of star and planet into β-cooling model, one evaluates the cooling source function as

$$\left(\frac{\partial u}{\partial t}\right)_{\rm cool} \approx \frac{u_{\rm eff}}{t_{\rm cool}} = -\frac{(u-u_{\rm irr,*}-u_{\rm irr,acc})}{t_{\rm cool}} = -\frac{(u-u_{\rm irr,*}-u_{\rm irr,p})\Omega_{\rm K}}{\beta}. \tag{5.8}$$

where the specific internal energy is calculated by $u = k_{\rm B}T/(\gamma - 1)\mu m_{\rm H}$.

5.2.2 Analytic Expactation

To analyze the accretion process, we describe it as the accumulation of surrounding material onto the circumplanetary disk that is going to migrate toward planet via viscous dissipation of angular momentum. The gravitational attraction of the planet is eligible to capture a shearing flow around the planet if the flow encounters an interaction cross-section. For the massive protoplanetary disk, the ratio of vertical scale-height to the Hill radius (i.e., $H_{\rm p}/R_{\rm H}$) is usually larger than the unity, and thereby the interaction cross-section can be approximated as a cross-section of the Hill sphere. Using this approximation, we express the accumulation rate of shearing flow into the Hill sphere as

$$\dot{M}_{\rm circ} \sim \int \rho_{\rm p} v_{\rm shear}\, {\rm d}A = 4\rho_{\rm p} R_{\rm H} \int_0^{\rm R_H} v_{\rm shear}\, {\rm d}x \sim \left(\frac{M_{\rm p}}{M_*}\right)\rho_{\rm p}\Omega_{\rm p} R_{\rm p}^3, \tag{5.9}$$

where the subscript p indicates disk quantities at the planet orbit, local radius is $d = R - \alpha_{\rm p}$, and the shearing flow $v_{\rm shear}$ is given by

$$v_{\rm shear} = \int_{R_{\rm p}}^{R_{\rm p}+R_{\rm H}} R\left(\frac{{\rm d}\,\Omega_{\rm K}}{{\rm d}\,R}\right){\rm d}R \approx -\frac{3}{2}\Omega_{\rm p} d. \tag{5.10}$$

We note that this accumulation rate over-estimates accretion rate onto the planet because surrounding material is accumulated in the timescale of local orbital frequency whereas a viscous timescale that relates to accretion rate is

$$t_{\rm vis,circ} \sim \frac{1}{\alpha_{\rm ss}\Omega_{\rm p}}\left(\frac{R_{\rm H}}{H_{\rm p}}\right)^2 > \Omega_{\rm p}^{-1}. \tag{5.11}$$

Thus, we suggest an accretion rate to be proportional to the accumulation rate with the ratio of timescales

$$\dot{M}_{\rm acc} \sim \dot{M}_{\rm circ} \times \frac{1}{\Omega_{\rm p} t_{\rm vis,circ}} \sim \alpha_{\rm ss}\left(\frac{M_{\rm p}}{M_*}\right)^{1/3}\rho_{\rm p} R_{\rm p} H_{\rm p}^2 \Omega_{\rm p}, \tag{5.12}$$

or substituting $\rho_{\rm p} \sim \Sigma_{\rm p}/(2H_{\rm p})$, we obtain

$$\dot{M}_{\rm acc} \sim \left(\frac{M_{\rm p}}{M_*}\right)^{1/3}\Sigma_{\rm p} R_{\rm p} c_{\rm s,p}, \tag{5.13}$$

where $c_{\rm s,p}$ is local sound speed. This analytic formula for the accretion rate implies that disk material is readily accreted onto the more massive planet and that the accretion is stimulated as planet migrates inward since the surface density and temperature rapidly increase.

To estimate the final mass of the planet via migration, however, we need to relate the accretion rate with migration rate. The phase of planet migration can be largely classified into type I and II cases depending on whether the planet makes disk open a gap, and the migration rate significantly changes by migration type. Until a protoplanet gains sufficient mass for gap opening (i.e., type I migration), it strongly couples with the gaseous flow, which generally results in negative resonance torque that makes the planet rapidly migrates inward. As the planet gradually increases mass, the coupling with gaseous flow become weaken because enhanced tidal interaction cleans disk material around planet orbit, so the planet stalls orbital evolution. After disk forms a distinct gap, we consider the planet then undergoes type II migration. During the type II migration, the planet trapped within the disk gap slowly moves toward host star in a viscous timescale of the disk.

There is uncertainty to determine a transition mass of the planet switching migration phase from type I to II case because of sequential processes of disk evolution, but Ward (1997) first suggested an analytic form of $M_{\rm trans} = 0.4\alpha_{\rm ss}^{2/3} h_p^{-1/3}$. Thereafter Bate et al. (2003) had found the previous definition was over-estimated in a few factors, so they differently calculated in $M_{\rm trans} = 1.8\, M_* h_{\rm p}^3$. By definition of Bate et al. (2003), we obtain the transition mass $M_{\rm tran} \approx 1.89\, M_{\rm J}$ with $h_{\rm p} = 0.1$ in our disk structure. Although the initial planet mass in our standard models (i.e., $M_{\rm p,init} = 2\, M_{\rm J}$) already surpasses the transition mass, there require a few dynamical timescales for the density perturbation by planet mass to propagate across the whole disk structure in the hydrostatic equilibrium. Therefore, the protoplanet will undergo the change of migration phase even if the protoplanet is massive enough for gap opening.

Considering the transition mass, Bate et al. (2003) provided an empirical form of the migration rate to be

$$v_{\rm mig} = \frac{v_{\rm migI}}{1+(M_{\rm p}/M_{\rm trans})^3} + \frac{v_{\rm migII}}{1+(M_{\rm p}/M_{\rm trans})^{-3}} \tag{5.14}$$

where migration velocities $v_{\rm mig}$ calculated by Tanaka et al. (2002) and Bate et al. (2003) are given by respectively,

$$v_{\rm migI} = -f\frac{M_{\rm p}(\alpha_{\rm p}^2\Sigma_{\rm p})}{M_*^2}h_{\rm p}^{-2}\alpha_{\rm p}\Omega_{\rm p}, \tag{5.15}$$

where $f \approx 3.9$ for the surface density profile $\Sigma \propto R^{-1}$ and

$$v_{\rm migII} = -\frac{3}{2}\alpha_{\rm ss}h_{\rm p}^2\alpha_{\rm p}\Omega_{\rm p}. \tag{5.16}$$

According to Bate et al. (2003), the migration rate converges to type II rate if the planet is massive than transition mass (i.e., $M_{\rm p}/M_{\rm trans} \gg 1$). Therefore, we approximate migration timescale as

$$t_{\rm mig} \sim \frac{R_{\rm p}}{v_{\rm mig}} \sim \frac{1}{\alpha_{\rm ss}\Omega_{\rm p}}\left(\frac{H_{\rm p}}{R_{\rm p}}\right)^{-2}. \tag{5.17}$$

Combining accretion rate and migration timescale, we estimate the mass growth to be

$$\delta M_{\rm mig} \sim \dot{M}_{\rm acc} \times t_{\rm mig} \sim \left(\frac{M_{\rm p}}{M_*}\right)^{1/3}\rho_{\rm p}R_{\rm p}^3, \tag{5.18}$$

which can be written in the relation of

$$\delta M_{\rm p} \propto M_{\rm p}^{1/3}R_{\rm p}^{3/2}T_{\rm p}^{-1/2}, \tag{5.19}$$

implying that the planet efficiently gains mass via accretion during migration if the planet is initially massive and formed at distant cold disk region. This result is well matched with our expectation that the more massive planet strongly attracts shearing flow to be gravitationally bound and that the colder disk material would be readily accreted onto the planet.

5.2.3 Planet Evolution via Migration

Overview of Planet Migration

Before introducing individual results of simulations, we outline the overall evolution of seed planet via migration. According to morphological features in **Figure 7.1-7**, we can classify the evolution sequence of the planet migration into three phases: **(1)** initial non-linear perturbation ($\lesssim 1\,\mathrm{kyrs}$) — gravitational perturbation on the relaxed disk by involved planet mass changes physical condition of its surrounding, **(2)** early linear phase ($\sim 1-3\,\mathrm{kyrs}$) — insufficient planet mass cannot largely perturbs disk density and only weakly derives spiral pattern on the disk, and **(3)** late non-linear phase — sufficient planet mass with accretion forms distinct spiral arms and circumplanetary disk, and then disk clears planet orbit (gap opening). From the different evolution phases, the planet differently achieves both mass growth and orbital evolution. Since the planet simultaneously evolves its mass and orbit as a result of migration, we need to understand the planet evolution in terms of mass growth and orbital change together. Here, a useful parameter to describe the planet evolution is the Hill radius ($R_{\mathrm{H}} \sim R_{\mathrm{p}} M_{\mathrm{p}}^{1/3}$). As the planet increases its mass and migrates, the change of Hill radius will show different slop depending on evolution phase. According to the **Figure 5.4**, the Hill radius does not largely change at the first phase because there is no efficient accretion flow and torques from the disk. However, after a thousand years (i.e., early linear phase), the planet suffers from gravitational torque by interacting with disk material and steadily enhances accretion flow onto it. So, we find the Hill radius rapidly decreases in this phase. As the disk-planet interaction form more dense non-linear structure on the disk (i.e., late non-linear phase), the planet stalls its orbital evolution and mass accretion by opened disk gap, allowing the Hill radius keep a plateau for the time.

The **Figure 5.5** describe sequential evolution of protoplanet from the migration in the plane of mass-orbital radius, and the **Figure 5.6** estimates the change of migration timescale. For each panel of a figure (totally four panels are shown), we draw

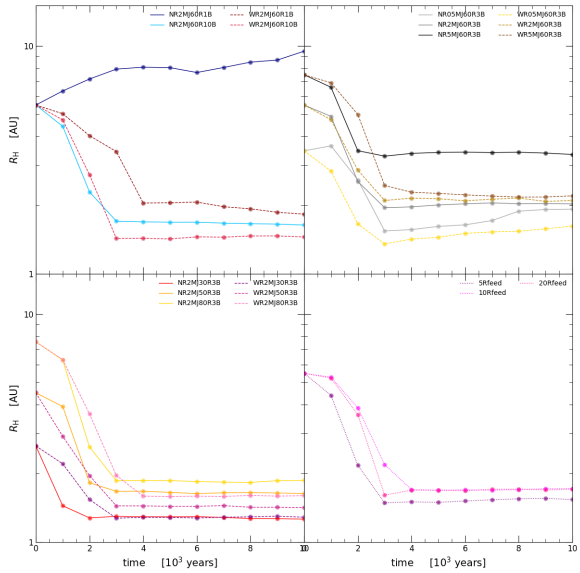

Figure 5.4: Change of Hill radius during planet migration: [LEFT-TOP] different β coefficients, [LEFT-BOTTOM] different initial orbital radii $a_{\mathrm{p,init}}$, [RIGHT-TOP] different initial masses $M_{\mathrm{p,init}}$, [RIGHT-BOTTOM] different feedback radius R_{feed}. Each marker indicates a time step of simulation for every thousand years, and dashed-lines are models with planet radiative feedback

comparable models only different in one parameter: each panel compares simulations with different β coefficients (left-top), different initial orbital radii $a_{\mathrm{p,init}}$ (left-bottom), different initial masses $M_{\mathrm{p,init}}$ (right-top), and different feedback radius R_{feed} (right-bottom). Each dot in the figures indicates simulation time step for every thousand years. The difference between solid-lines and dashed-lines is whether the model involves radiative feedback from planet accretion. In the **Figure 5.5**, we find protoplanets evolve into massive gas giants ranging in mass between a few to ten Jupiter mass and orbiting a few AU away from the host star. So, we judge the protoplanet would finally turn into a hot Jupiter from the migration rather than become stellar object (e.g. brown dwarf or another low-mass companion star). Also, the planet usually tends to

undergo inward migration except for in the **NR2MJ60R1B** model. Our result differs from previous numerical studies which predicted proplanet formed from gravitational instability surly grows in mass above the range of gas giant. On this difference, we will discuss in the next section in detail. In the **Figure 5.6**. the migration occurs in a rather short period ($\sim 10^3\,\mathrm{yrs}$) compared with a life-time of the protoplanetary disk ($\sim 10\,\mathrm{Myrs}$). The migration rate is calculated by

$$t_{\mathrm{mig}} = \frac{\dot{R}_{\mathrm{p}}}{R_{\mathrm{p}}}. \tag{5.20}$$

Considering analytic estimation of migration rate, the planet migrates inward in the rate of type I migration, but the morphology of protoplanetary disk (refer to **Figure 7.1-7**) argues the disk open a gap within a thousand year like type II migration. The rapid migration rate in the simulation results from the strong interaction between the planet and massive disk which induces strong inward torque on the planet, whereas the analytic estimation assumed the disk mass is relatively ignorable than stellar mass. The rapid migration rate in massive protoplanetary disk is also commonly shown in previous studies. For the role of radiative feedback from planet accretion, as shown in **Figure 5.5** and **Figure 5.6**, we understand it delays the final orbital settlement of the planet and largely suppresses growth in mass. This is because the planet radiation does not only interrupts planet accretion by heating its surrounding but also weakens resonance torques which repel disk material from the planet orbit.

Mass Growth and Orbital Evolution without Planet Radiative Feedback

We first examine migration of non-radiative protoplanets which are embedded in the disk with different cooling rate, located at different orbital radii, and have different initial mass; see **Figure 5.7-9**. The non-radiative one means that the protoplanet does not radiate accreted energy as feedback to the surrounding. We typically name the models as following **Table 7.1-3**. Except for the variable parameter, the identical parameter setup is used in each run. The following figures in this section show mass growth and orbital evolution of the planet for the run.

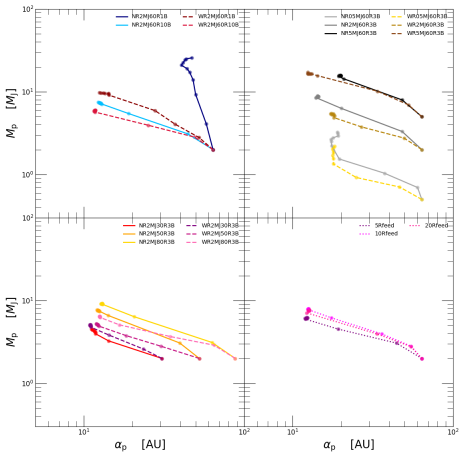

Figure 5.5: Planet evolution via migration in the space of Mass growth versus Orbital radius: [LEFT-TOP] different β coefficients, [LEFT-BOTTOM] different initial orbital radii $a_{\rm p,init}$, [RIGHT-TOP] different initial masses $M_{\rm p,init}$, [RIGHT-BOTTOM] different feedback radius $R_{\rm feed}$. Each marker indicates a time step of simulation for every thousand years, and dashed-lines are models with planet radiative feedback.

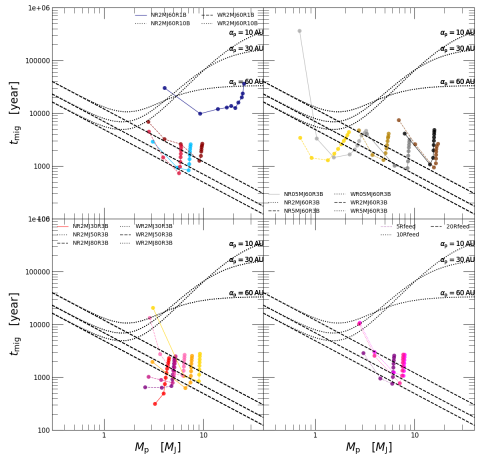

Figure 5.6: Migration timescale as a function of planet mass: [LEFT-TOP] different β coefficients, [LEFT-BOTTOM] different initial orbital radii $a_{\rm p,init}$, [RIGHT-TOP] different initial masses $M_{\rm p,init}$, [RIGHT-BOTTOM] different feedback radius $R_{\rm feed}$. We plot analytic migration timescales (Bate et al. 2003) with several orbital radii ($\alpha_{\rm p}$ = 10, 30, and 60 AU) as a reference, taking $h_{\rm p}$ = 0.1 and $\Sigma_{\rm p} = 50\,{\rm g\,cm^{-2}}$. Each marker indicates a time step of simulation for every thousand years, and dashed-lines are models with planet radiative feedback

From the comparison of different cooling rate models (see **Figure 5.7** and **Figure 7.1**), we find that threshold of β coefficient for the disk to be unstable becomes around $\beta \approx 3$ in this work. This value is similar to previous study of Deng et al. (2018); although they tested local instability, but the global instability in the disk should precede.

As seen in **Figure 7.1**, rapid cooling rate in the cold disk model (i.e. $\beta = 1$) makes the disk unstable and sustains strong spiral arms derived by planet until the end of run which is considered for the planet to be fully evolved. On the other hands, the warmer disks (i.e., $\beta \geq 3$) display spiral arms smoothed as wound ring pattern that exists at the overall disk radii. The strength of spiral arms results from how the planet strongly interacts with disk. This implies the disk that features strong spiral arms is going to form strong accretion flow onto the planet. As we expect, the cold disk model (i.e., **NR2MJ60R1B**) opens a gap within relatively shorter timescale ($\sim 1 - 1.5\,\mathrm{kyrs}$) and forms a wide and apparent gap on the disk. During migration, the planet in the cold disk increases mass with rather rapid accretion rate ($\sim 10^{-3} - 10^{-2}\,M_{\mathrm{J}}\,\mathrm{yr}^{-1}$). Other planets in a warmer disk (i.e., $\beta \gtrsim 3$) accretes disk material with lower accretion rate of $10^{-4} - 10^{-3}\,M_{\mathrm{J}}\,\mathrm{yr}^{-1}$ for longer timescale of gap opening ($\sim 1.5 - 2\,\mathrm{kyrs}$). So the planet in the cold disk accomplishes sufficient mass growth to become a stellar object like a brown dwarf (i.e., $M_{\mathrm{p}} \gtrsim 12\,M_{\mathrm{J}}$) as a result. After the disk ends gap opening, the planet in the cold disk only steadily accretes disk material via streams from gap edges unlike planets in the warmer disk discontinue accretion. The streams are thought to be caused due to a high-pressure gradient at the gap edges of cold disk. The final mass growth in different cooling rate models concludes the warmer disk results in more suppressed accretion flow onto the planet. This tendency is understood by the accretion flow cannot easily be bound onto the planet due to inefficient cooling rate.

The unstable disk structure even makes planet migrate outward. The outward migration is not a usual feature in the planet migration in a massive protoplanetary disk, but we have uncommonly found in previous studies by different reasons The outward migration shown in the unstable disk already rose by Cloutier & Lin (2013). They found the outward migration may be caused by gravitational instability at the edge of unstable disk gap. The edge mode instability exerts outward net tidal torque on the planet, allowing it moves outward. So, we witness the planet embedded in the cold disk shows unstable structure and outward migration at the same time. In the stable

disk, the evolved planets finally settle nearby the central star ($R_{\rm p,f} \approx 10\,{\rm AU}$).

The high accretion rate for a gas giant in a massive cold disk matches an SPH result of Stamatellos et al. 2017 that treated disk cooling by calculating radiative transfer equation (Stamatellos et al. 2007). While the idealized β-cooling prescription roughly estimates disk cooling rate with orbital frequency, the method of Stamatellos et al. 2007 approximates a proper disk temperature by considering disk components, such as ions, ices, and dust, but results in a quite cold disk environment. Compared with β-cooling models, Nayakshin et al. (2018) that used $0.2\,M_{\odot}$ of a disk with $\beta = 0.1$ shows similar accretion rate with our cold disk model, but their disk structure exhibits lower surface density with $R_{\rm d} = 300\,{\rm AU}$. According to code comparison test for planet migration (Fletcher et al. 2019), they concluded that the GIZMO measures the lowest accretion rate in identical simulation domain with $\beta = 10$, and then final mass growth of other SPH methods are at least twice or three times larger than the result of GIZMO. Therefore, we understand a disk in the GIZMO domain is relatively warmer than the disks described in other SPH methods. In addition, a gas giant treated by other SPH methods will not avoid to grow up its mass above brown dwarf regime ($M_{\rm p} \sim 11.6 - 16\,M_{\rm J}$ in Spiegel et al. 2011) if disk structure features a critical β coefficient ($\beta_{\rm crit} \approx 3$) in Deng et al (2017) to trigger gravitational instability in the disk.

A distant initial orbital radius lets the planet initially evolve at sparse disk region, delaying orbital settlement; the timescale of type II migration is proportional to the square of planet orbital separation (Bate et al. 2003). Despite initially low accretion rate due to sparse density, the protoplanet initially orbiting distant region is going to achieve larger mass growth during longer epoch of the migration. For the non-radiative planet models with different initial orbital radius (**NR2MJ-30R/50R/60R/80R-3B**), they commonly present an averaged accretion rate of $10^{-3}\,M_{\rm J}\,{\rm yr}^{-1}$, and their migration timescale seems to be proportional to initial orbital radius; see **Figure 5.8**. The planets reach their final mass growth from a few to ten Jupiter mass by different ini-

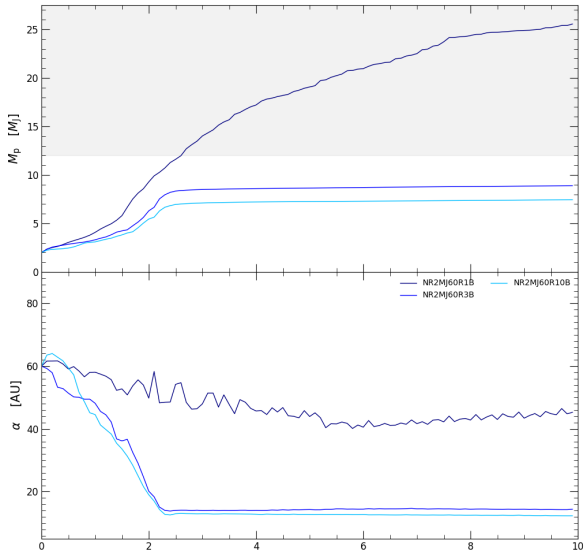

Figure 5.7: The evolution of planets embedded in disk with different cooling rates: [TOP] Mass growth, [BOTTOM] Orbital separation

tial orbital radius. However, we can hardly expect the planet is formed not only in an innermost region of which the temperature is extremely high due to strong stellar radiation but also in an outmost region with sparse disk density. Intermediate disk region only satisfies enough low temperature and high density for the disk to be gravitationally unstable. In this work, we confirm that Toomre Q parameter falls below 1.5 in the orbits between $50 - 80\,\mathrm{AU}$. Thus we rule out **NR2MJ30R3B** that evaluates a final mass growth as below $5\,M_\mathrm{J}$ and find that the non-radiative planets will increase mass in a high mass range of $8 - 10\,M_\mathrm{J}$ in our disk structure. Stamatellos et al. 2017 also examined migration models of the radiative planet with a varying initial orbital radius between $50 - 80\,\mathrm{AU}$, but all planets evolve to the massive objects of which masses range beyond $15\,M_\mathrm{J}$. It may be inevitable for the massive objects to become brown

dwarfs, turning on core deuterium burning (Spiegel et al. 2011). Therefore, the migration of radiative protoplanet described by GIZMO may be feasible to provide various types of a gas giant from low to high Jupiter mass if a protoplanetary disk has different mass and size.

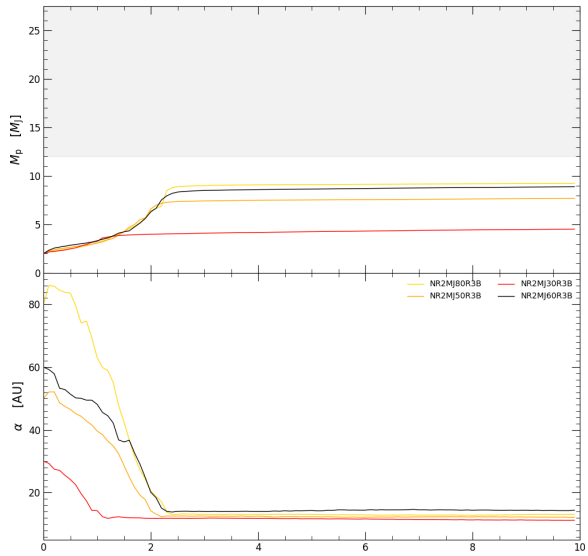

Figure 5.8: The evolution of planets with different initial orbital radii: [TOP] Mass growth, [BOTTOM] Orbital separation.

We lastly preform various types of planet migration with different initial masses. Depending upon how effectively the disk opens a gap via gravitational perturbation of planet mass, one determines the type of migration. A massive protoplanet without radiation (**NR5MJ60R3B**) makes the disk shortly begin to open a gap (within $\sim 0.5\,\mathrm{kyrs}$) and grows its mass with rapid accretion rate ($\sim 10^{-3} - 10^{-2}\,M_\mathrm{J}\,\mathrm{yr}^{-1}$), so it directly undergoes the phase of type II migration. Conversely, a low mass protoplanet (**NR05MJ60R3B**) cannot open a clear gap on the disk until it settles in a certain

orbit and very slowly accretes disk material similar to type I migration. An ordinary non-radiative planet with $M_{\rm p} = 2\,M_{\rm J}$ (**NR2MJ60R3B**) is first embedded in the disk and migrates inward without rapid accretion. When its mass reaches $\sim 5\,M_{\rm J}$, the mass growth is sufficient for the disk to effectively opens a gap, and the planet undergoes type II migration; we call this phase the transitional migration. These models show the different variation of accretion rate according to their migration phase. The massive planet cannot largely perturb disk density for an orbital period ($\sim 0.5\,{\rm kyrs}$) but soon clears disk material around its orbit, resulting in gap opening and corresponding rapid accretion rate. The low mass planet cannot initially accrete sufficient disk material for $3.5\,{\rm kyrs}$, but its accretion rate slightly increases after the disk forms a weak gap; the planet grows in mass to only $\sim 3\,M_{\rm J}$ for $10\,{\rm kyrs}$. The ordinary planet grows in mass with slow accretion rate ($\sim 10^{-4}\,M_{\rm J}\,{\rm yr}^{-1}$) for the type I migration ($\sim 1.5\,{\rm kyrs}$) but thereafter rapidly increases mass ($\sim 10^{-2}\,M_{\rm J}\,{\rm yr}^{-1}$) by switching its orbital evolution into type II phase.

Mass Growth and Orbital Evolution with Planet Radiative Feedback

We in this section repeat the planet migration in identical parameter space including accretion feedback of the planet. The **Figure 5.10**, **12**, and **13** shows mass growth and orbital evolution of the radiative planet, and we draw results of the non-radiative case together as faint lines for reference. In addition, we perform planet migration varying feedback radius in order to compare the effect of radiation strength onto the planet evolution; see **Figure 5.13**.

First, comparing the two cold disk models (**NR2MJ60R1B** and **WR2MJ60R1B**), the planet radiation is identified as an important process in suppressing mass growth of the planet and in delaying gap formation. This is because the planet radiation heats accretion flow, preventing the flow readily approaches toward the planet due to additional pressure gradient, and then the radiative planet takes more time to achieve sufficient mass for gap formation. Also, we witness the radiative feedback stabilize

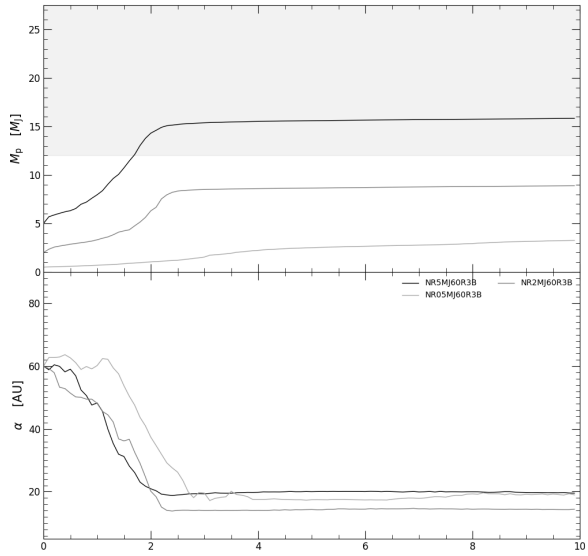

Figure 5.9: The evolution of planets with different initial mass: [TOP] Mass growth, [BOTTOM] Orbital separation.

unstable structure seen in previous section. In the **Figure 5.10** and **Figure 7.3**, the **WR2MJ60R1B** forms a gap relatively slower than than **NR2MJ60R1B** ($\sim 3.5\,\mathrm{kyrs}$) and has a clear gap with no edge-mode instability. Since the no edge-mode instability stalls keeping accretion flow after gap formation is complete, the **WR2MJ60R1B** model discontinues mass growth of the planet after disk ends gap formation compared with **NR2MJ60R1B** (see stalled mass growth of **WR2MJ60R1B** after $t = 3.5\,\mathrm{kyr}$). Not only suppressed mass growth after gap opening, but the stabilized gap edge removes outward torque and makes radiative planet undergo inward migration. At the end, the radiative planet embedded in the cold disk does not exceed threshold mass for being brown dwarf ($M_{\mathrm{p,f}} \sim 10\,M_{\mathrm{J}}$) and moves to vicinity of the host star ($R_{\mathrm{p,f}} \sim 10\,\mathrm{AU}$).

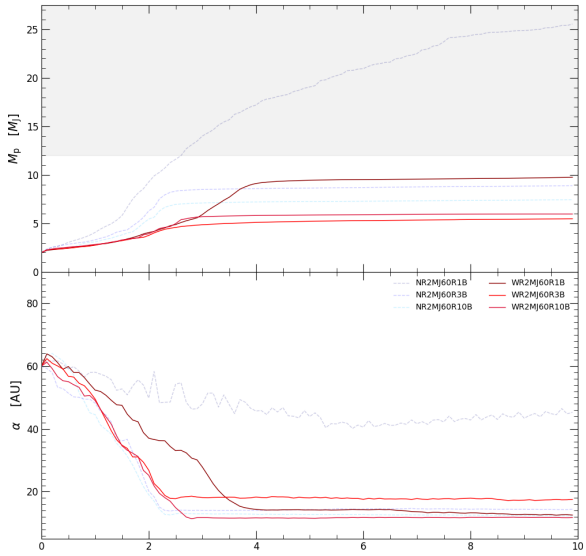

Figure 5.10: The evolution of planets with different feedback radius: [TOP] Mass growth, [BOTTOM] Orbital separation.

In the following figure, we can identify the role of planet radiation. The **Figure 5.11** displays temperature profile on $R-z$ plane around the planet at $t = 1500\,\mathrm{yr}$. The left panel shows non-radiative planet in the cold disk and right one is the case when planet radiates. Here, the stream lines over the temperature profile indicates relative vertical velocity field to the planet motion which is scaled with $v_{10000} = 0.1\,\mathrm{km}/s$). The white solid line is the Hill sphere, and the dashed-dot line surrounds the area of the half Hill radius. In the figure, the central star locates at left side of the each panel. The gas flow passing mid-plane around the planet indicates circumplanetary disk, and the flow vortices shown in the vicinity of the planet are caused by non-linear structure like spiral arms.

For the non-radiative planet in the cold disk, accretion flow rapidly approaches

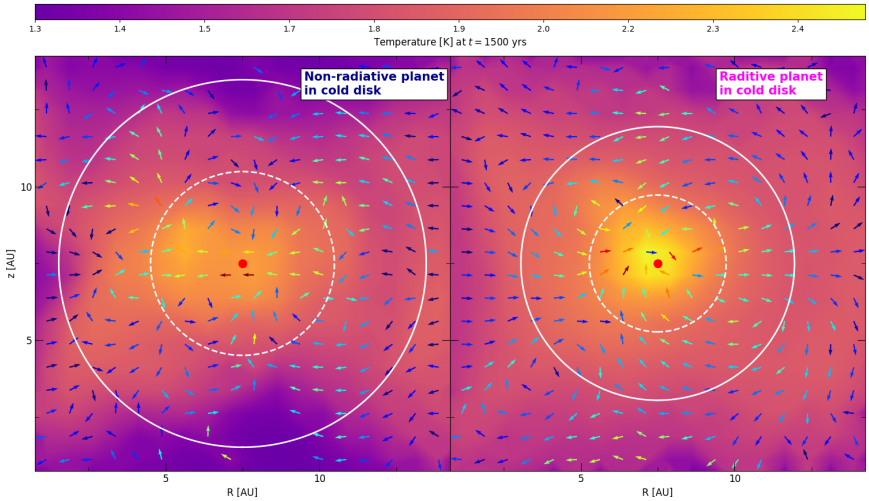

Figure 5.11: Temperature field in vertical plane around planet orbit at $t = 1500\,\mathrm{yr}$: $v_{10000} = (\Delta v/0.1\,\mathrm{km\,cm^{-1}})$

mid-plane entering circumplanetary disk and also be directly accreted onto the planet through its poles. Apparent accretion flow through polar direction is due to the efficient cooling rate of the disk that smoothes pressure gradient around the planet. However, if the radiative feedback is included, the planet develops hotter environment than non-radiative case (about a few hundred Kelvin). Thus, the accretion flow around the planet poles is deflected by high pressure gradient supported with radiative heating. Also, we witness the vortices is weaken because radiative heating loosen spiral arms and bulge like structure around the radiative planet.

In the warm disk models (**NR2MJ60R3B** and **WR2MJ60R1B**), both protoplanets do not evolve above the regime of brown dwarf. Taking into account radiative feedback, however, radiative planet grows only to $\sim 5\,M_J$ and delays gap opening as $0.5\,\mathrm{kyr}$. In the hot disk models (**NR2MJ60R10B** and **WR2MJ60R10B**), the natural hot disk environment makes the planet radiation less crucial in the role of suppressing planet accretion; we find the difference of mass growth between **NR2MJ60R10B**

and **WR2MJ60R10B** is only $\sim 1\,M_{\rm J}$. These results raise an argument on the role of planet radiation. In previous studies (typically, Stamatellos et al. 2018), they argued the planet radiation takes a crucial role in planet evolution because the planet reaches quite different fate during the migration depending on whether the model includes planet radiation.However, the planet radiation may not be a crucial factor in the disk-planet interaction unless the cooling rate is efficient as rapid as the local orbital period.

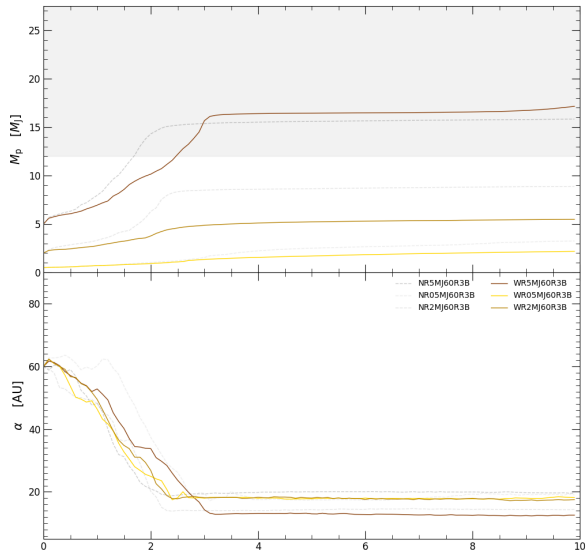

Figure 5.12: The evolution of planets with different feedback radius: [TOP] Mass growth, [BOTTOM] Orbital separation.

According to **Figure 5.12** and **Figure 5.13**, the radiative feedback of the planet do not vary orbital separation compared with non-radiative cases but largely reduce final mass growth. However, we witness the **WR5MJ60R3B** model shows the planet radiation from massive planet yields enhanced mass growth during migration. This mysterious results is understood by strong interaction between disk and massive planet

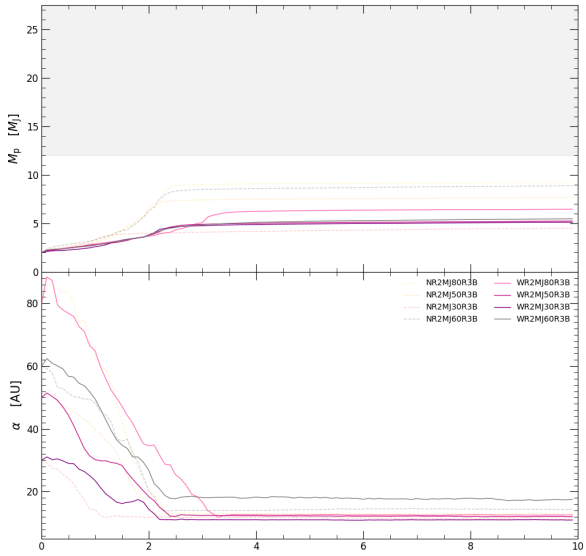

Figure 5.13: The evolution of planets with different feedback radius: [TOP] Mass growth, [BOTTOM] Orbital separation.

body. Although the planet radiation in the **WR5MJ60R3B** decreases the accretion rate, the massive radiative planet undergoes migration for a extended period, sustaining massive circumplanetary disk around it. In the **Figure 5.14**, both the **NR5MJ60R3B** and **WR5MJ60R3B** models results that their planets forms a massive circumplanetary disk of which mass exceeds $\sim 0.1\,M_{\rm J}$. While the non-radiative planet migrates ($\sim 1.5 - 2\,{\rm kyrs}$), the amount of disk material accumulated within Hill sphere of **NR5MJ60R3B** is about $2 - 3$ times heavier than **WR5MJ60R3B**. After the non-radiative planet ends migration, **NR5MJ60R3B** drops the mass of circumplanetary disk below $10^{-2}\,M_{\rm J}$, but the mass of circumplanetary disk in **WR5MJ60R3B** surpasses **WR5MJ60R3B** at $1.5\,{\rm kyrs}$. The circumplanetary disk around massive radiative planet sustains for $\sim 3\,{\rm kyrs}$. Therefore, the radiative planet can achieve more mass

growth in the case of massive planet.

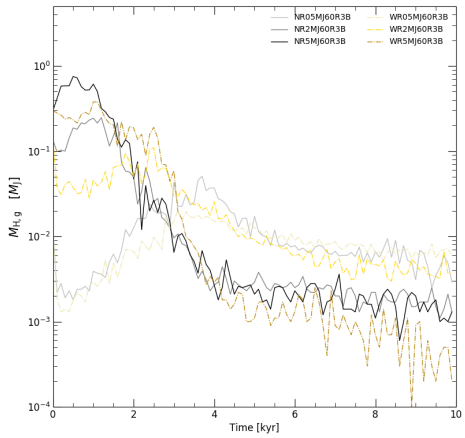

Figure 5.14: Total mass of disk material within Hill sphere: the details on how we identify the circumplanetary material is explained in next section.

The **Figure 5.15** is results of simulations varying feedback radius up to 20 $R_{\rm feed}$. As the planet feedback is enhanced (i.e., $R_{\rm feed}$ decreases), the accretion flow suffers from strong radiative heating which prevents the flow is easily captured within accretion area. Thus, final mass growth of planet is gradually reduced as feedback radius increases. Whereas the mass growth seems to be related with feedback radius, orbital separation and migration timescale irregularly changes. We guess irregular orbital evolution of planet depending on the feedback radius is caused by collective effects of complex tidal torques.

5.2.4 Morphological Features

Circumplanetary Disk

To classify the circumplanetary disk, we simple the gaseous particles within the Hill radius around the planet and verify whether they are gravitationally bound to the planet

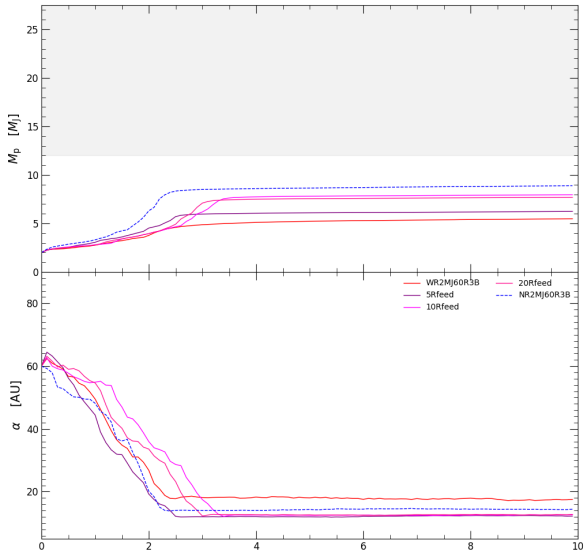

Figure 5.15: The evolution of planets with different feedback radius: [TOP] Mass growth, [BOTTOM] Orbital separation.

by checking $E_{\rm tot} = E_{\rm grav} + E_{\rm kin} < 0$. Referring to column density profile in **Figure 7.1-7**, we know the bound mass to the planet comprises of the circumplanetary disk and a part of spiral arms. However, we simply consider it represents the scale of the circumplanetary disk by assuming negligible spiral arms mass. In the different disk circumstance, the circumplanetary disk diversely varies its mass in the range of $10^{-3} - 10^{-1}\ M_{\rm J}$ for the migration, and the migration model exhibiting a higher accretion rate reasonably tends to form dense circumplanetary disk (high accretion rate is caused by internal processes of massive accumulated disk material as the circumplanetary disk). Since the size of the circumplanetary disk is proportional to the Hill radius, we find the disk become larger as its mass is more massive. The mass of circumplanetary disk is reduced when the planet radiation is taken into account. This is considered that the

disk material cannot be readily bound to the planet gravity due to additional thermal pressure of the planet radiation. In stead of the decreased mass, the circumplanetary disk exists around the planet for relatively longer period; this is related to delayed gap formation.

Prior to investigate the properties of circumplanetary disk, we understand the properties can be dependent on simulation resolution typically in the particle-based method, due to poor resolution around the planet (also see discussion in Stamatellos 2018). Assuming the circumplanetary disk with one tenth of Jupiter mass distributes over $10\,\mathrm{AU}$, one predicts the environment of circumplanetary disk is described by a few thousands gaseous particles and then resolved within a few smoothing length scale ($\sim 1\,\mathrm{AU}$). This impliies that the simulation result can resolve the circumplanetary disk in the level of minimum resolution but the local fluctuation do not satisfy the resolution. Meanwhile, as we alluded in previous section, this work has intrinsic shortcoming to investigate thermal properties around the planet due to the approximations of β-cooling and Shakura-Sunyaev α viscosity. Nevertheless, we believe that this work is available qualitatively to explain diverse environment around the planet in the various conditions of the overall protoplanetary disk.

In order to compare the diverse characteristics of circumplanetary disk in various disk properties, we select following six models: **NR2MJ60R1B** (cold disk model), **WR2MJ60R1B** (cold disk model with planet radiation), **NR5MJ60R3B** (massive planet model), **NR2MJ80R3B** (model of long initial orbital period), **NR2MJ60R3B** (standard model), and **WR2MJ60R3B** (standard model with planet radiation).

The **Figure 5.11** shows logarithmic column density profile around the planet orbit at $t = 2500\,\mathrm{yr}$ (left) and at $t = 5000\,\mathrm{yr}$ (right). Velocity field in the co-rotating frame of the planet is over-plotted on the density profile as stream lines of which color indicates the magnitude of logarithmic speed. The solid and dashed-dot line shows Hill and a half of Hill area respectively, and the central red dot is planet position. The gas flow executes horseshoe orbit due to disk-planet interaction. Most gas flow results in

clearing planet orbit by flowing along the spiral arms, but the flow nearby the planet is captured with the Hill sphere. The gas flow within the Hill sphere forms a circumplanetary disk around the planet as a result of angular momentum conservation and is linked to the inner and outer disk with the spiral arms. Whereas the previous studies of planet migration without accretion (e.g. Baruteau et al. 2011; Lin et al 2012; Malik et al. 2015) shows the formation of relatively larger and growing circumplanetary disk (their circumplanetary disks fully fill with Hill sphere), all the models in this work commonly form the circumplanetary disk within the half Hill radius until the protoplanetary disk is opening a gap (see the snapshots at $t = 2500\,\mathrm{yr}$). This is because the circumplanetary disk is going to be accreted onto the planet (this is also seen in other accretion models, Humphries 2018; Stamatellos 2015; 2018). In the two dimensional studies (Lubow et al. 1999; D'Angelo et al. 2002; Ayliffe et al. 2008), sub-spiral arms driven by infall shock flow was witnessed in the circumplanetary disk, but Bate 2003 proved the spiral arms is loosen by allowing vertical motion of the flow. So we only witness the bulged circumplanetary disk. At the snapshots of $t = 5000\,\mathrm{yr}$ in which we consider the disk and planet enough evolves, the protoplanetary disk clears gas flow around planet orbit, and only radiative planets sustain the vague circumplanetary disk. Notable thing is **NR2MJ60R1B** still has a dense circumplanetary disk due to steady infall streams from inner and outer disk edges. This implies that the circumplanetary disk may survive from the disk-planet evolution if the disk features efficient cooling rate (i.e. $\beta \ll 1$) and planet radiation is not threatening. Although we do not aim to investigate the ring system of gas giants, the condition for the circumplanetary disk to survive can be issue on the formation of the ring system that is considered to originate from the circumplanetary disk. As we find in various migration models, the circumplanetary disk seems to relate with efficiency of disk cooling, and the efficient cooling rate will contradictorily enhance planet radiation resulted from mass accretion. Even if we neglect the planet radiation, the efficient disk cooling allows the gas giant to evolve into super gas giants, contrary to the consequence of the observation that find the ring

system in low mass gas giants. Also other disk dispersal effect, such as photoevaporation and magneto-outflow, will interrupt the formation of circumplanetary disk. So far people cannot models the formation process of the ring system but expect the issue would be solved by involving the physics of dust-gas coupling or allowing multi-planet system.

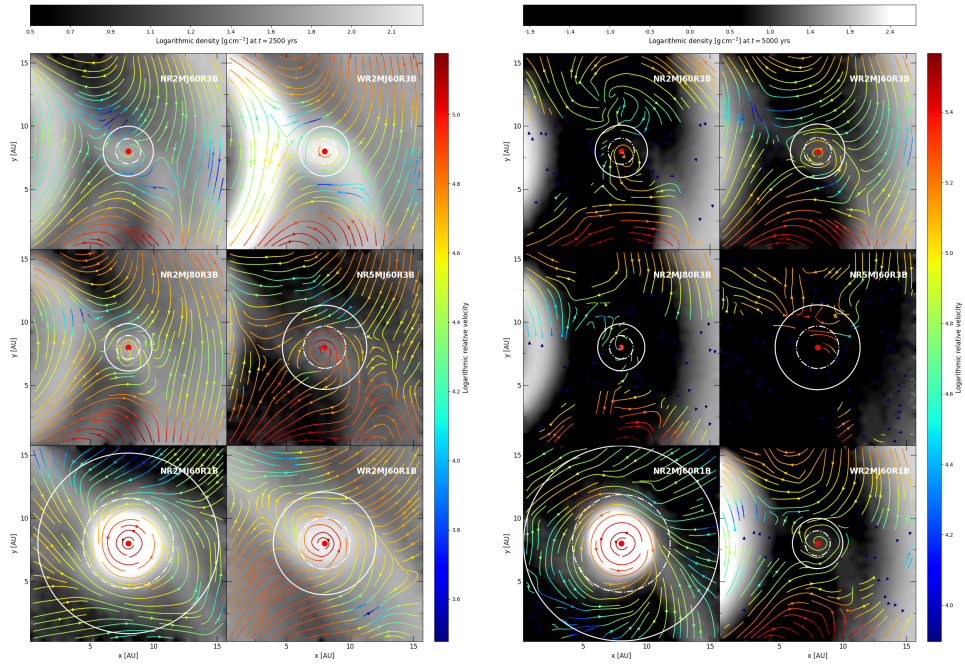

Figure 5.16: Relative velocity field of gas flow around the planet at $t = 2500\,\mathrm{yr}$ (left) and at $t = 5000\,\mathrm{yr}$ (right): we plot the planet as red dot and the size of Hill sphere as solid circle, and dashed circle is scaled with $R_{\mathrm{H}}/2$.

In the **Figure 5.13**, we plot azimuthally-averaged thermal properties in the plant frame at $t = 1500, 2500, 5000\,\mathrm{yr}$. Each snapshots is considered to represent migration phases in which the disk begins open the gap ($t = 1500\,\mathrm{yr}$), the disk halts the gap opening ($t = 2500\,\mathrm{yr}$), and the disk have fully evolved and relaxed ($t = 5000\,\mathrm{yr}$). The open circles in the figures indicate the radius of Hill sphere. On the third panel

in **Figure 5.13**, we introduce a relative specific energy e defined as $e = -(u + \Phi)$, where u is specific internal energy, $\Phi = GM_{\rm p}/\Delta r$ is relative gravitational potential. Using the gradient of relative specific energy, we judge how the circumstance around the planet make the flow to migrate toward the planet. At the early phase of the planet migration (i.e., $t = 1500\,{\rm yr}$), the **NR2MJ60R1B** forms remarkably dense circumplanetary disk via efficient cooling rate, and **NR2MJ80R3B** shows lowest surface density distribution due to its sparse density of the surrounding. The gravitational heating via intensive disk-planet interaction in the **NR5MJ60R3B** causes relatively high temperature at early phase. Compared between models with and without planet radiation, we find the planet radiation makes the overall disk more relatively hotter (the difference is significant in the cold disk models). Thereby the disk model without planet radiation features the broad distribution of positive relative specific energy while the positive area is limited within the Hill radius if the planet radiative feedback is taken into account. This feature implies that the planet radiation interrupts the disk flow to be bound to the planet. After the disk open the gap ($t > 2500\,{\rm yr}$), the models without planet radiation form more clear gap on the disk than with planet radiation. As we have seen in **Figure 5.11**, the conservative circumplanetary disk in the **NR2MJ60R1B** appears as high surface density around the planet. Also, we find that the **NR2MJ80R3B** and **NR5MJ60R3B** achieve sufficient mass growth, forming clear disk gap. As the accretion is stalled, the area of positive relative specific energy is expanded over the Hill area in the models with planet feedback.

Disk Gap Opening and Spiral Arms

By running simulations in various situations, we are able to understand the mass and orbital evolution of gas giants due to their gravitational interactions with protoplanetary disks. In this section, we try to relate between simulation results to observable quantities like planet luminosity, disk gap, and spiral pattern. Due to development of high resolution infrared observation, we have detected large population of young

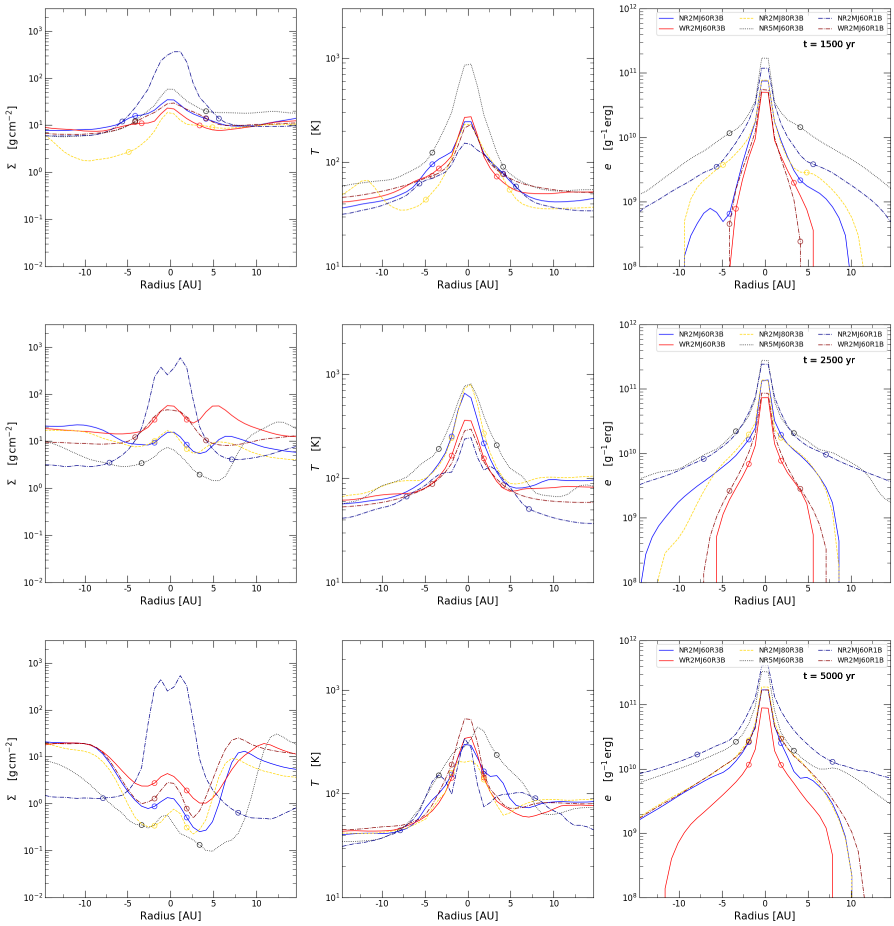

Figure 5.17: Thermal properties of the circumplanetary disk $t = 1500\,\mathrm{yr}$ (top), at $t = 5000\,\mathrm{yr}$ (middle), and at $t = 8000\,\mathrm{yr}$ (bottom): we consider the disk fully develops gap after $t = 8000\,\mathrm{yr}$.

stellar system hosting cirumstellar disk and become possible to resolve internal disk structure. Especially, commonly found disk gap, ring or spiral pattern give us evidence for the existence of protoplanet and corresponding physical quantities. So if we can define quantitative relation between observables and disk parameters, it will be a great contribution to revealing the origins of planets and planetary systems.

Evaluating planet luminosity caused by accretion, we find the planet luminosity

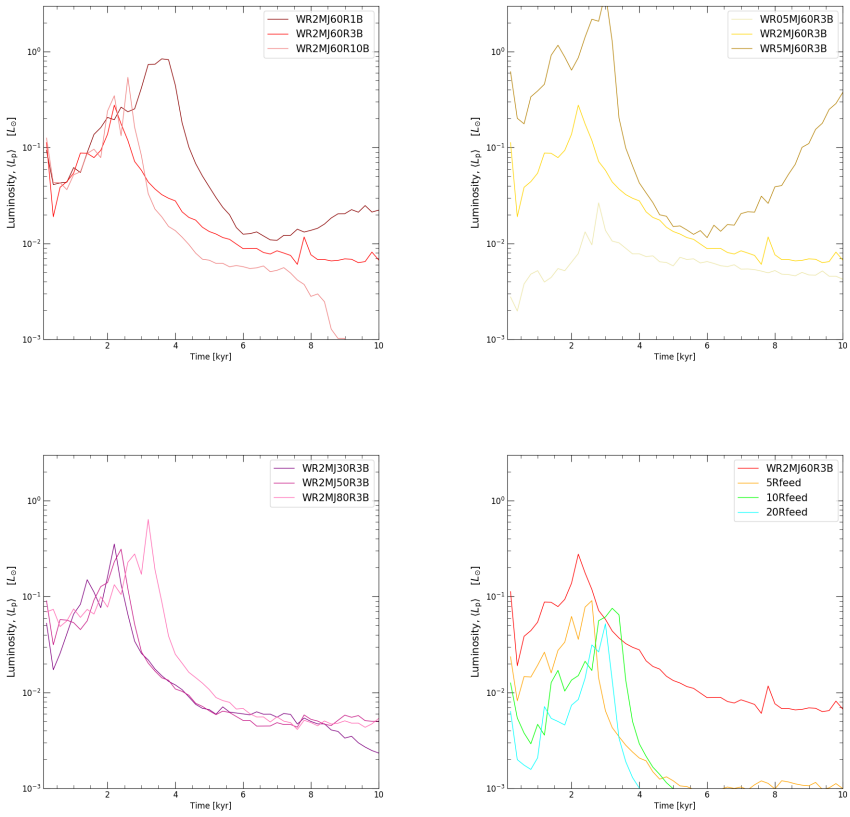

Figure 5.18: Planet Luminosity as accretion feedback: [LEFT-TOP] different β coefficients, [LEFT-BOTTOM] different initial orbital radii $a_{\rm p,init}$, [RIGHT-TOP] different initial masses $M_{\rm p,init}$, [RIGHT-BOTTOM] different feedback radius $R_{\rm feed}$.

is enhanced as comparable as solar luminosity; see **Figure 5.**. As we have seen in previous section, planet luminosity is estimated as much as mass accretion rate ($\dot{M}_{\rm p}$). Thus, massive protoplanet embedded in a cold disk will shine brightest. However, the strength of planet luminosity is open to vary due to uncertainty on the feedback radius ($R_{\rm feed}$). In the right-bottom panel of **Figure 5.**, the planet luminosity is changed in several times magnitude. Although we understand the accreting planet may be difficult to detect because the accretion onto the planet only last a few thousand years ($\lesssim 2-$

3 kyrs), there is a reliable possibility that the accreting planets are detected around a very young stellar object. However, we fortunately know representative examples that found accreting planet, such as young stellar system of **LkCa-15** (Sallum et al. 2015) and **PDS 70** (Haffert et al. 2019).

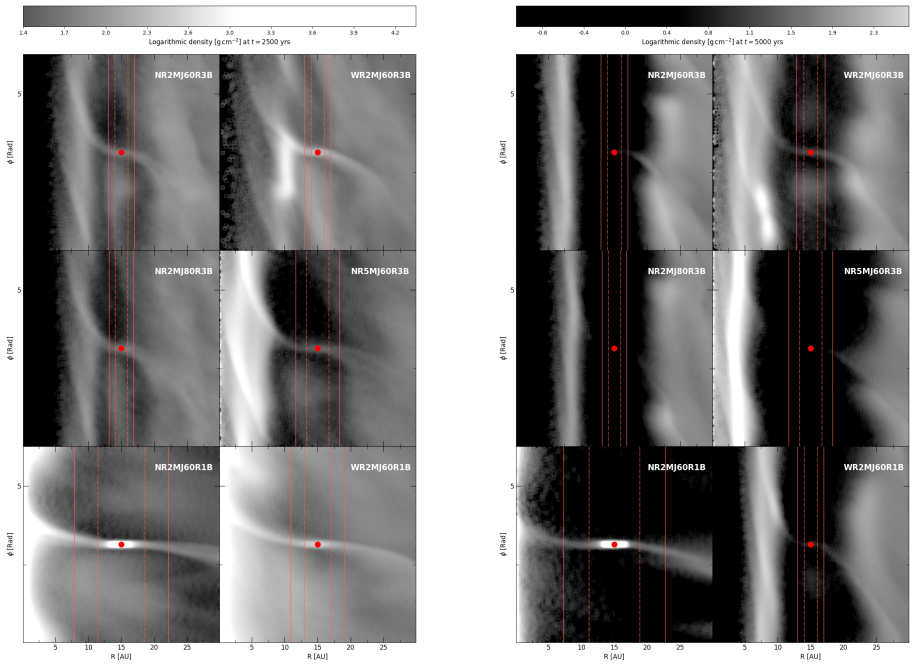

Figure 5.19: Surface density in $R - \phi$ space at $t = 2500\,\mathrm{yr}$ (left) and at $t = 5000\,\mathrm{yr}$ (right): we plot the planet as red dot, and vertical red lines indicate Hill area.

Astronomers are capable to directly observe disk structures by imaging from infrared observation these days, but there is a great diversity in defining disk gap or spiral pattern. In spite of diverse definition, the best way to define them will eventually be to understand them by using physical quantities of the disk and planet. Kanagawa et al. (2015) first tried to relate between disk-planet quantities and observables. They

defined a dimensionless parameter K' which is

$$K' = \frac{1}{\alpha_{\rm ss}} \left(\frac{M_{\rm p}}{M_*} \right)^2 \left(\frac{H_{\rm p}}{R_{\rm p}} \right)^{-3} \tag{5.21}$$

and found empirical relation from 2D steady disk simulation. Their suggestion using planet mass and orbital radius is quite reasonable because the gap width is determined by corresponding size of Hill radius. They measured the gap width to be radial distance between two points of which surface density is a half of initial surface density at planet orbit. As a result, they gave the relation to be

$$\Delta = \alpha K'^{\beta} = 0.41\, K'^{1/4}. \tag{5.22}$$

The shortcomings of their results are that they examined the simulation with no self-gravity of the disk and accretion process and that the results has intrinsic limitation to deal with vertical evolution due to limited dimension of domain. So, we expect results of this work would suggest improved relation than previous 2D numerical studies.

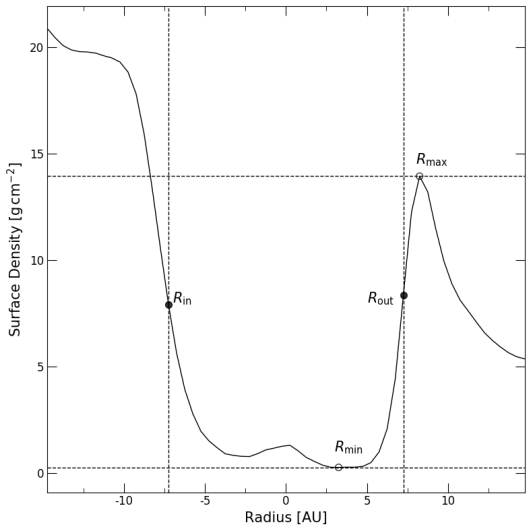

Figure 5.20: Demonstration of definition of gap width in this work in terms of $R_{\rm in}$, $R_{\rm out}$, $R_{\rm min}$, and $R_{\rm max}$

In order to measure a disk gap width, we require how the width is defined. According to individual studies, they differently defines the gap width using surface density profile or velocity dispersion. In this work, we use own definition of disk gap width given by

$$\Delta = \frac{R_{\rm out} - R_{\rm in}}{R_{\rm p}}, \tag{5.23}$$

where $R_{\rm out}$ and $R_{\rm in}$ are inner and outer boundary, respectively. The boundaries are found as following steps: We first find minimum and maximum peak of surface density around the planet orbit. Since the surface density increase at inner radii, we search the maximum at outer radii from the planet. The minimum peak is also confined within the disk gap. Defining the orbital radius of minimum and maximum peaks, we calculate medium of surface density $\Sigma_{\rm med} = (\Sigma_{\rm max} - \Sigma_{\rm min})$ and find corresponding nearest inner and outer orbital radius. Then, we define the radii of which surface density is $\Sigma_{\rm med}$ as boundaries.

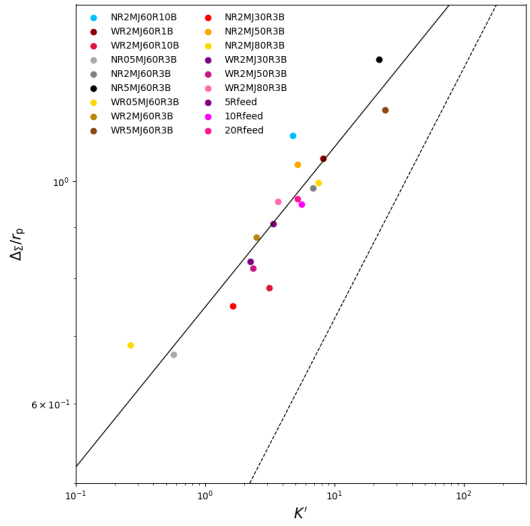

Figure 5.21: Disk gap width against dimensionless parameter K': The solid line is best-fit of this work and the dashed line follows fitting line by Kanagawa et al. (2015).

With the above measurement for gap width, we plot the relation of disk gap against the parameter K' in **Figure 5.**. The best fitting for this work follows

$$\Delta_{\rm my} = 0.75\, K'^{0.16}. \tag{5.24}$$

We believe that relatively modest change of $\Delta_{\rm my}$ against K' results from different dimension of the simulation. While we let the planet undergoes dynamical evolution varying its mass and orbital radius, final orbits in various situation relatively converge to $R_{\rm p,f} \sim 10\,{\rm AU}$ and the gap formation is determined after the planet fully grows in mass. Therefore, we understand the gap width is dominantly given as a function of planet mass; change of stellar mass is negligible.

Chapter 6

Summary and Conclusion

We study diverse evolutions of Jovian planet ($M_{\rm p} > 1\,M_{\rm J}$) formed in massive protoplanetary disk ($M_{\rm d} > 0.1\,M_{*}$). Depending upon how the disk and planet dynamically interacts, the protoplanet yields different mass growth and orbital evolution. In addition, we find that planet migration with radiative feedback leads the disk to delay the epoch of gap formation and to suppress accretion flow onto the planet. As a results, the planets in various situations evolves from massive gas giant to sub-brown dwarf orbiting nearby the host star ($R_{\rm p,f} \sim 10\,{\rm AU}$). Understanding the effects of radiative feedback on orbital evolution is not an easy task because the disk physics sensitively varies depending on the thermal properties of the disk, but we understand the planet radiation delays orbital settlement as like as gap formation through this work. The planet population of this work in the space of mass and orbital radius explains the existence of hot Jupiter is considered to be caused through planet migration. We also confirmed the GIZMO code features hotter thermal condition in identical simulation setup compared with previous numerical studies (c.f., Stamatellos 2015, Stamatellos et al. 2018)

A shortcoming of our simulation is disk cooling process is artificially prescribed with β-cooling model. Since the β-cooling model estimates disk cooling rate in comparable timescale of global orbital frequency, local cooling rate is necessarily underestimated. Thus the disk material that exists in spiral arms and circumplanetary disks

cannot cool down enough to be efficiently accreted onto the planet, resulting in suppressed mass growth of the planet. Furthermore, the cooling rate that slows as orbital radius increases makes the inner disk material to be more efficiently accreted onto the planet than the outer disk material, allowing the planet to necessarily migrates inward. The inevitable inward migration due to β-cooling prescription commonly appears in previous studies (e.g. Baruteau et al. 2011; Malik et al. 2015; Nayakshin & Cha 2013; Humphries & Nayakshin 2018). So we are hard to witness outward migration in the simulations with β-cooling model. Consequently, all planets except **NR2MJ60R1B** for finally settle in nearby inner cavity of the host star ($\sim$ 10 AU,) rather than fall into central region. This boundary for final orbital radius is considered as resolution of simulation setup. An alternative method for β-cooling is radiative transfer method suggested by Stamatellos (2007), but as we have seen in the comparison of mass growth, this has the limitation in that the internal structure of the protoplanetary disk is veiled from observation and the method consequently predicts a freezing disk temperature. With more accurate cooling process in the over-dense structures, we may understand diverse type of gas giants with its mass and orbital radius.

Although this work only focuses on disk-planet interaction and radiative feedback from star and planet, the evolution of protoplanet may result in more diverse type of object if we consider effects of other internal processes and magnetic field. Among these possibility, the photo-evaporation is considered to be a important factor in disk distribution. Since the strong flux from host star disperses disk material in early phase within short period, predictable range in mass growth during planet migration will shift below range, so the planets exhibiting high accretion rate during migration (e.g., **NR2MJ60R1B**, **NR5MJ60R3B**, and **WR5MJ60R3B**) are evitable to turn into stellar object.

Chapter 7

FIGURES AND TABLES

7.1 Figures

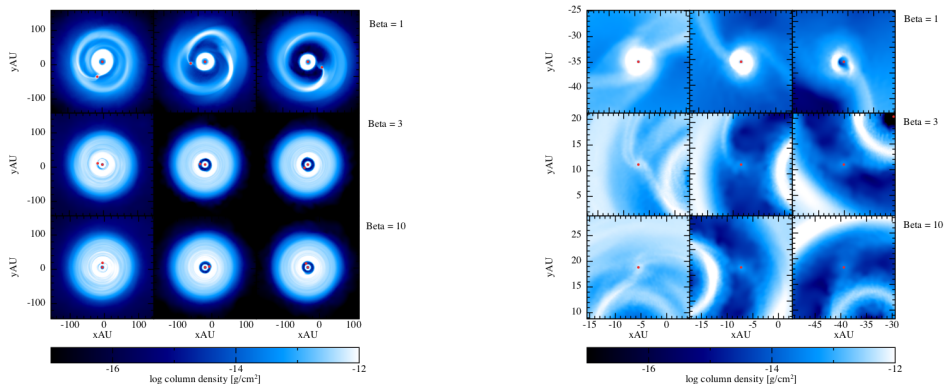

Figure 7.1: [LEFT] Logarithmic disk column densities of different β coefficient models without planet radiation feedback at $t = 2.5, 5.0, 7.5\,\mathrm{kyrs}$ from left to right, and [RIGHT] Zoom-in plot of disk surroundings in $20\,\mathrm{AU} \times 20\,\mathrm{AU}$ box. Red dots indicates the central star and planet.

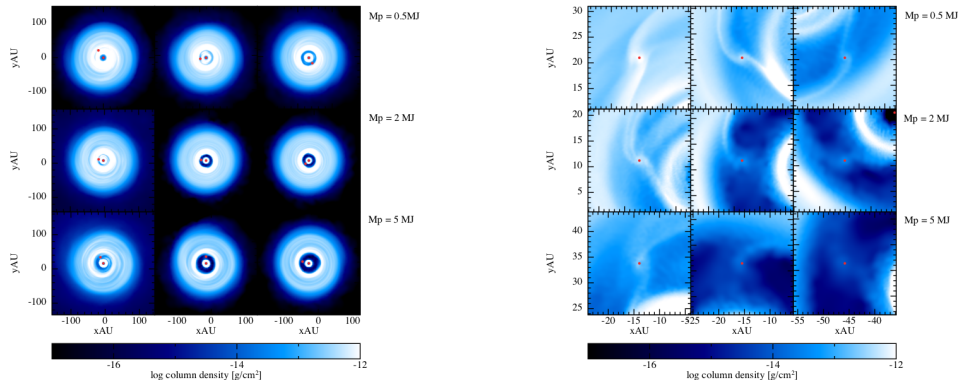

Figure 7.2: [LEFT] Logarithmic disk column densities of different initial mass $M_{\rm p,init}$ models without planet radiation feedback at $t = 2.5, 5.0, 7.5\,\rm kyrs$ from left to right, and [RIGHT] Zoom-in plot of disk surroundings in $20\,\rm AU \times 20\,AU$ box. Red dots indicates the central star and planet.

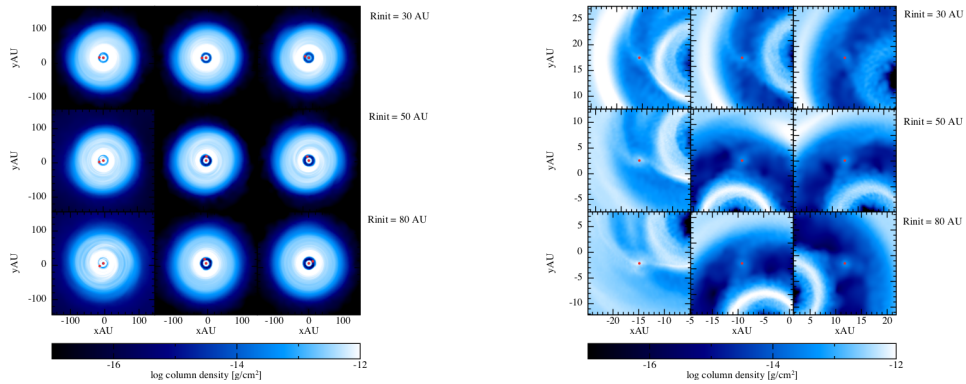

Figure 7.3: [LEFT] Logarithmic disk column densities of different initial orbital separation $\alpha_{\rm init}$ models without planet radiation feedback at $t = 2.5, 5.0, 7.5\,\rm kyrs$ from left to right, and [RIGHT] Zoom-in plot of disk surroundings in $20\,\rm AU \times 20\,AU$ box. Red dots indicates the central star and planet.

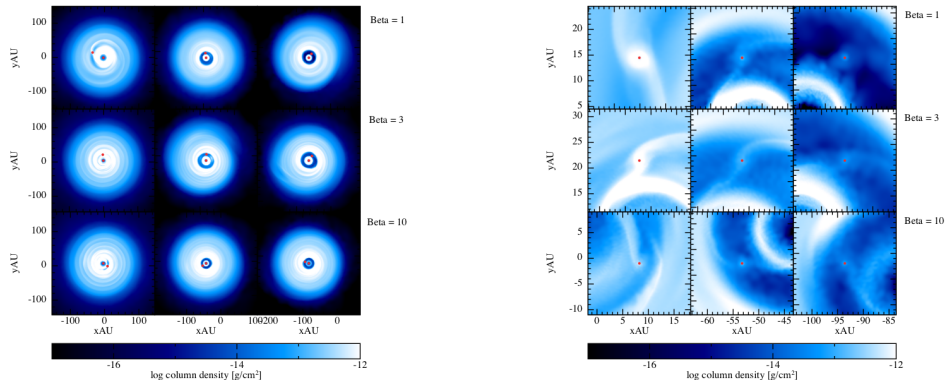

Figure 7.4: [LEFT] Logarithmic disk column densities of different β coefficient models with planet radiation feedback at $t = 2.5, 5.0, 7.5\,\mathrm{kyrs}$ from left to right, and [RIGHT] Zoom-in plot of disk surroundings in $20\,\mathrm{AU} \times 20\,\mathrm{AU}$ box. Red dots indicates the central star and planet.

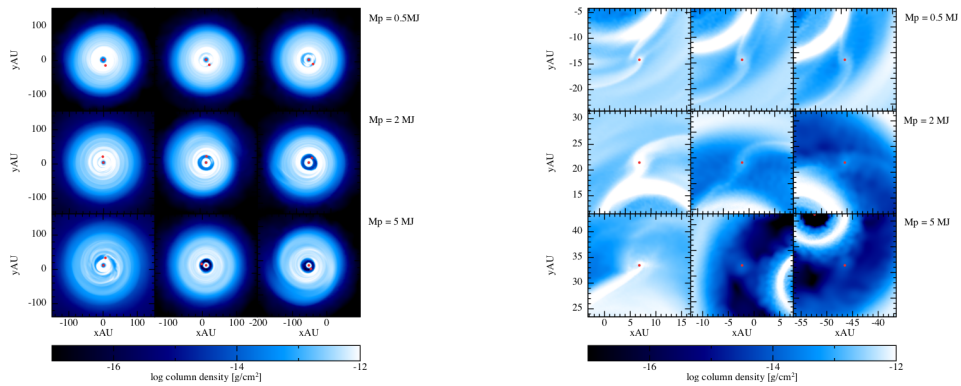

Figure 7.5: [LEFT] Logarithmic disk column densities of different initial mass $M_{\mathrm{p,init}}$ models with planet radiation feedback at $t = 2.5, 5.0, 7.5\,\mathrm{kyrs}$ from left to right, and [RIGHT] Zoom-in plot of disk surroundings in $20\,\mathrm{AU} \times 20\,\mathrm{AU}$ box. Red dots indicates the central star and planet.

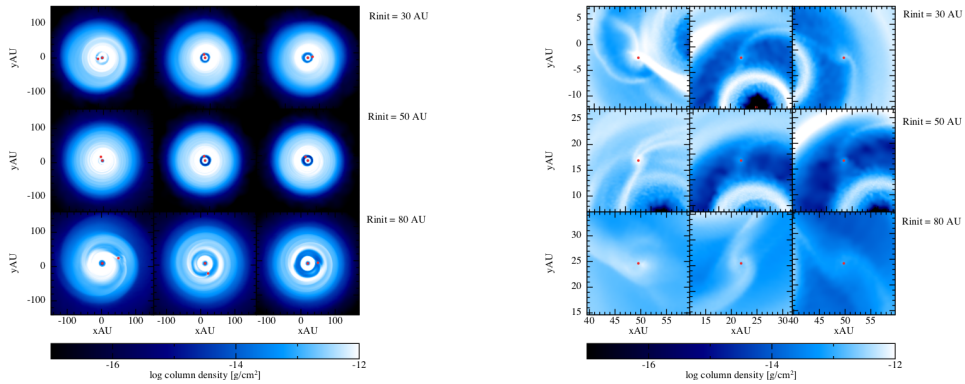

Figure 7.6: [LEFT] Logarithmic disk column densities of different initial orbital separation $\alpha_{\rm init}$ models with planet radiation feedback at $t = 2.5, 5.0, 7.5\,{\rm kyrs}$ from left to right, and [RIGHT] Zoom-in plot of disk surroundings in $20\,{\rm AU} \times 20\,{\rm AU}$ box. Red dots indicates the central star and planet.

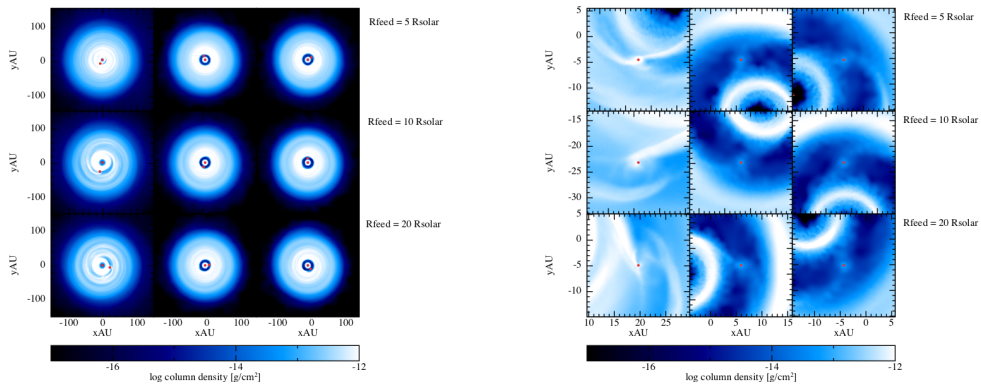

Figure 7.7: [LEFT] Logarithmic disk column densities of different feedback radius $R_{\rm feed}$ models with planet radiation feedback at $t = 2.5, 5.0, 7.5\,{\rm kyrs}$ from left to right, and [RIGHT] Zoom-in plot of disk surroundings in $20\,{\rm AU} \times 20\,{\rm AU}$ box. Red dots indicates the central star and planet.

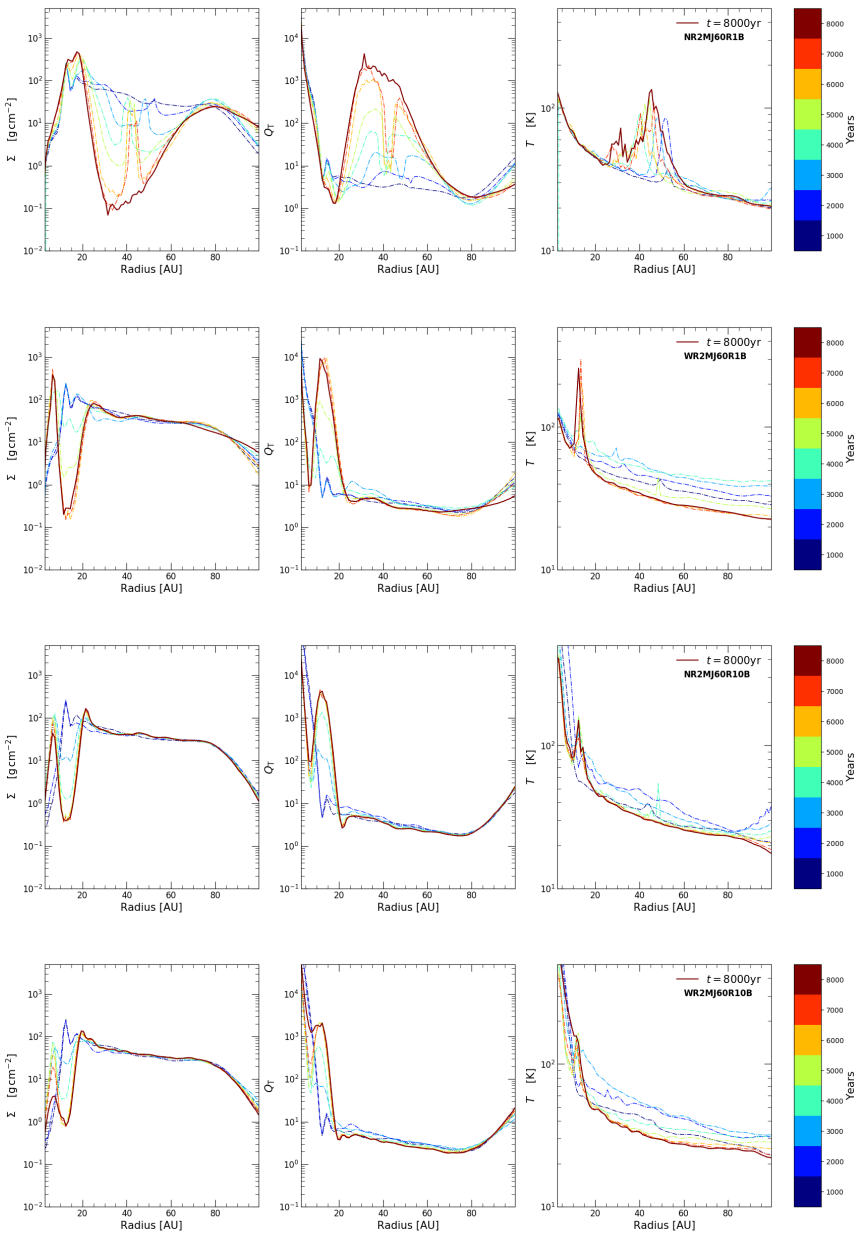

Figure 7.8: Evolution of disk thermal properties with different β coefficient: [LEFT] surface density, [MIDDLE] Toomre Q parameter, [RIGHT] temperature. We plot both two models with and without planet radiative feedback for comparison.

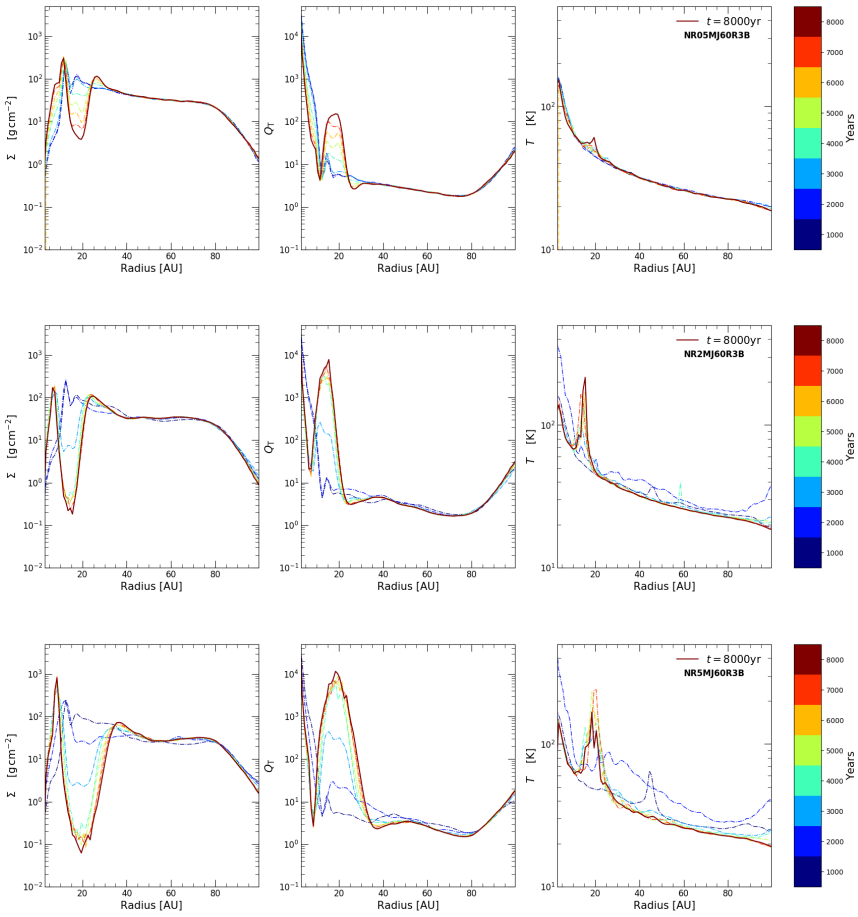

Figure 7.9: Evolution of disk thermal properties with different initial mass: [LEFT] surface density, [MIDDLE] Toomre Q parameter, [RIGHT] temperature. Here we only plot models without planet radiative feedback.

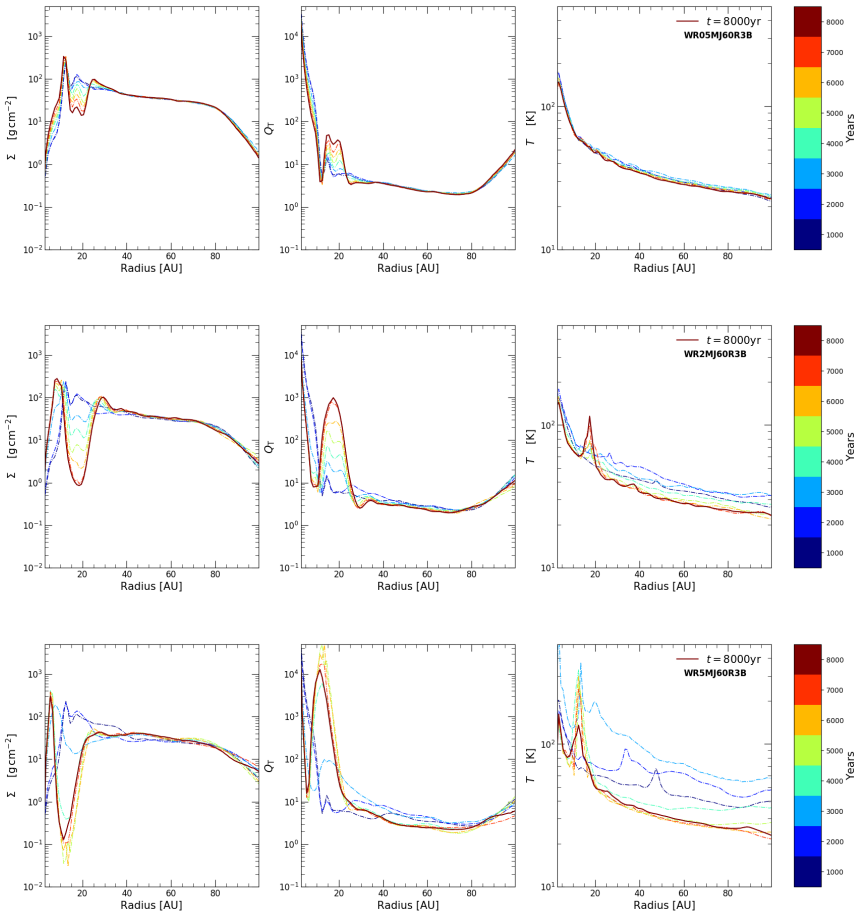

Figure 7.10: Evolution of disk thermal properties with different initial mass: [LEFT] surface density, [MIDDLE] Toomre Q parameter, [RIGHT] temperature. Here we only plot models with planet radiative feedback.

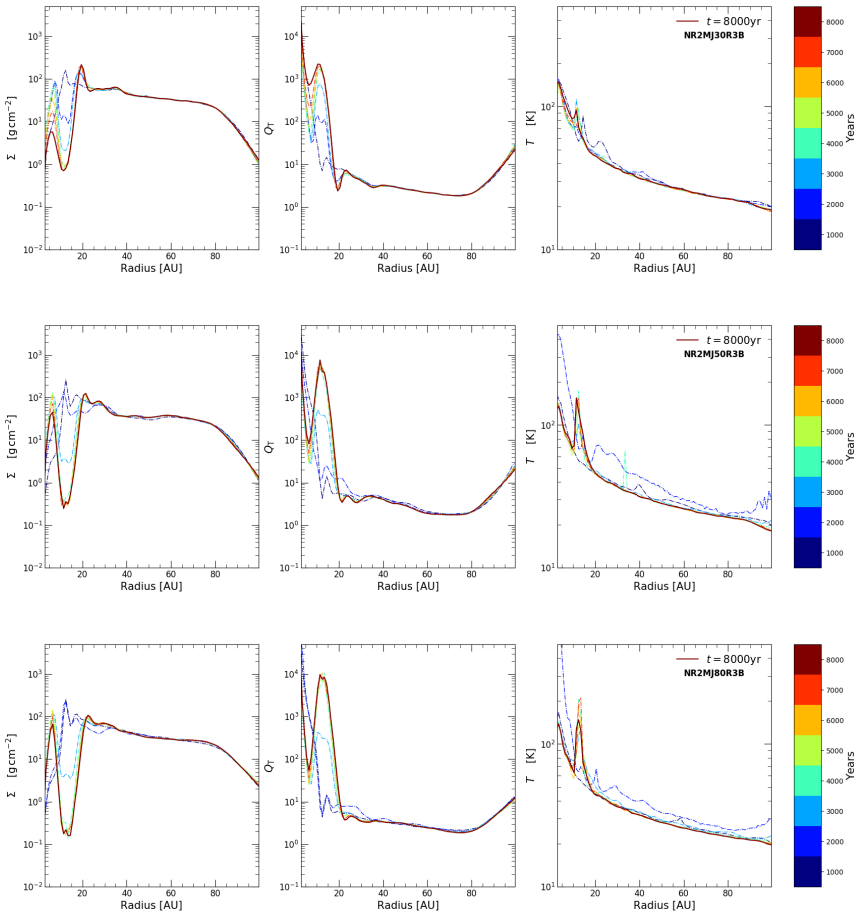

Figure 7.11: Evolution of disk thermal properties with different initial orbital radius: [LEFT] surface density, [MIDDLE] Toomre Q parameter, [RIGHT] temperature. Here we only plot models without planet radiative feedback.

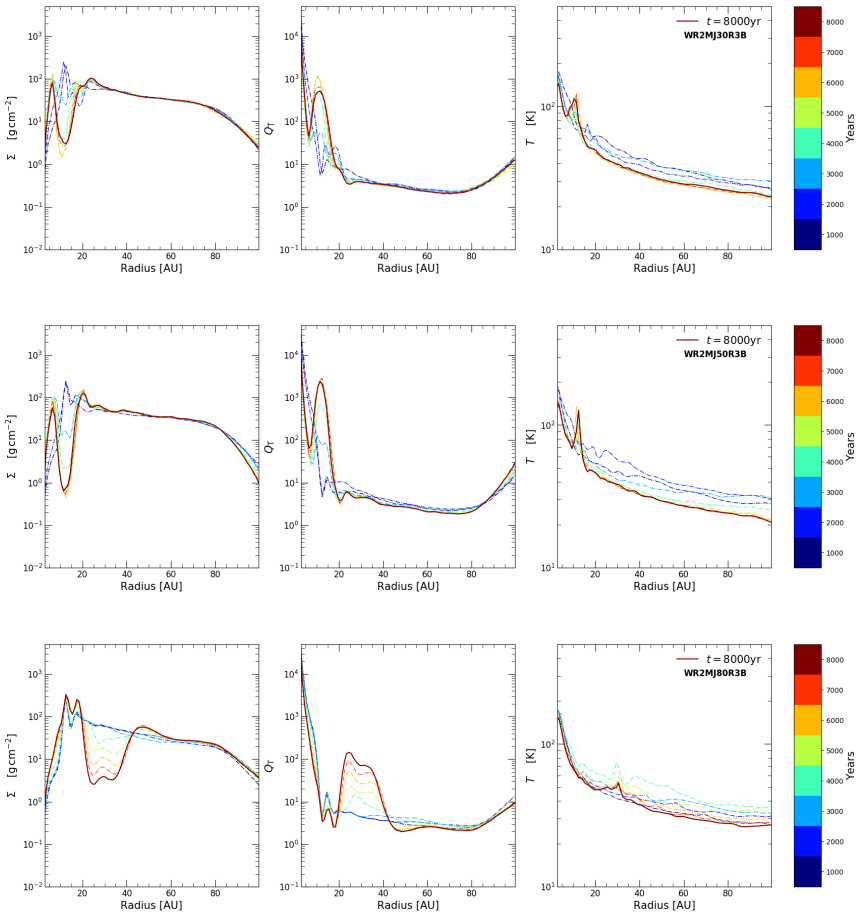

Figure 7.12: Evolution of disk thermal properties with different initial orbital radius: [LEFT] surface density, [MIDDLE] Toomre Q parameter, [RIGHT] temperature. Here we only plot models with planet radiative feedback.

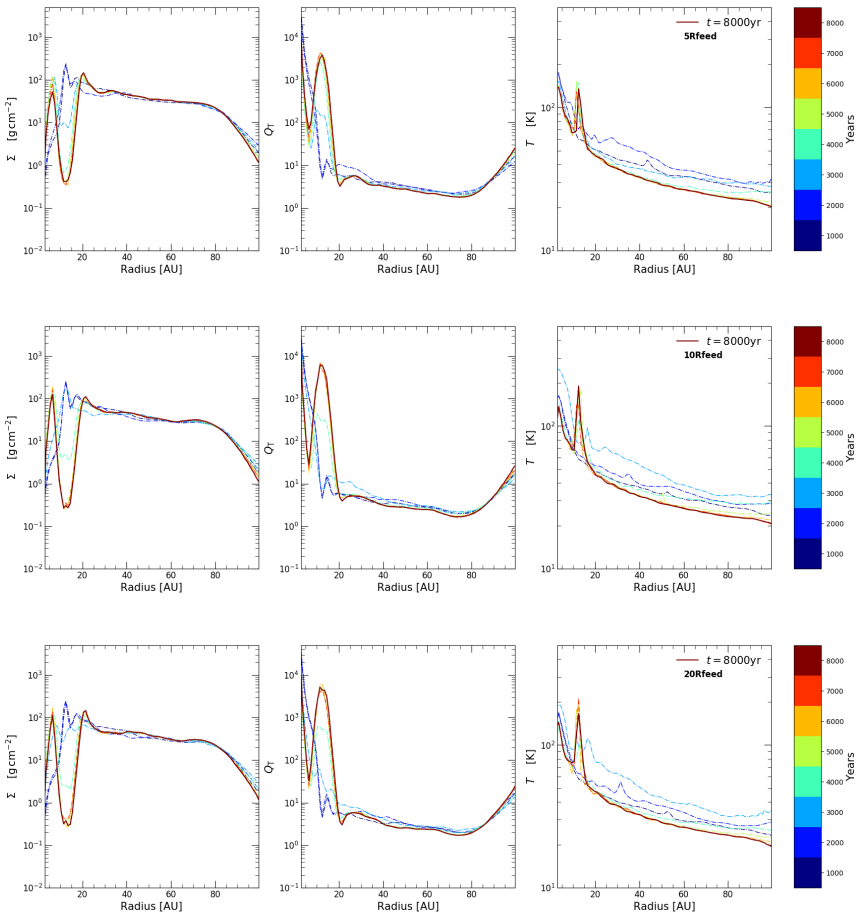

Figure 7.13: Evolution of disk thermal properties with different feedback radius: [LEFT] surface density, [MIDDLE] Toomre Q parameter, [RIGHT] temperature.

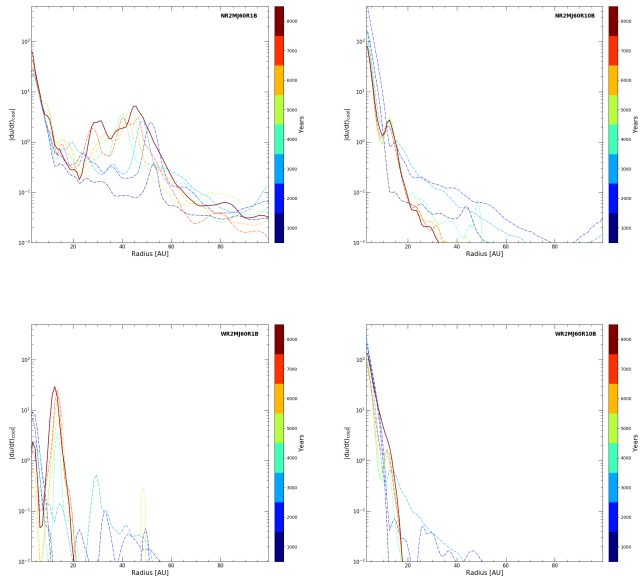

Figure 7.14: Azimuthally averaged β-cooling rate $|\mathrm{d}u/\mathrm{dt}|_{\mathrm{cool}}$. we take account of stellar radiation and radiative feedback from planet if it is considered in model

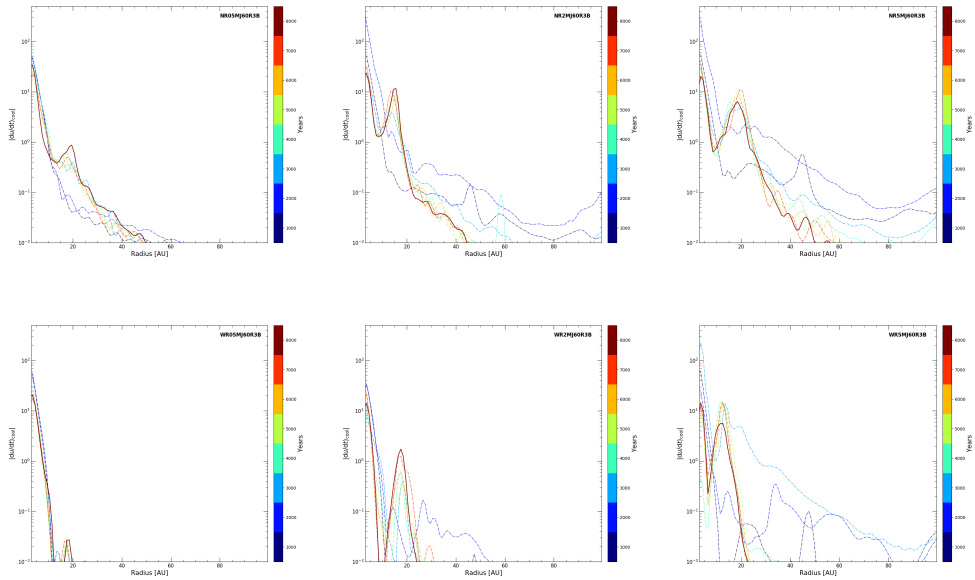

Figure 7.15: Azimuthally averaged β-cooling rate $|\mathrm{d}u/\mathrm{d}t|_{\mathrm{cool}}$. we take account of stellar radiation and radiative feedback from planet if it is considered in model

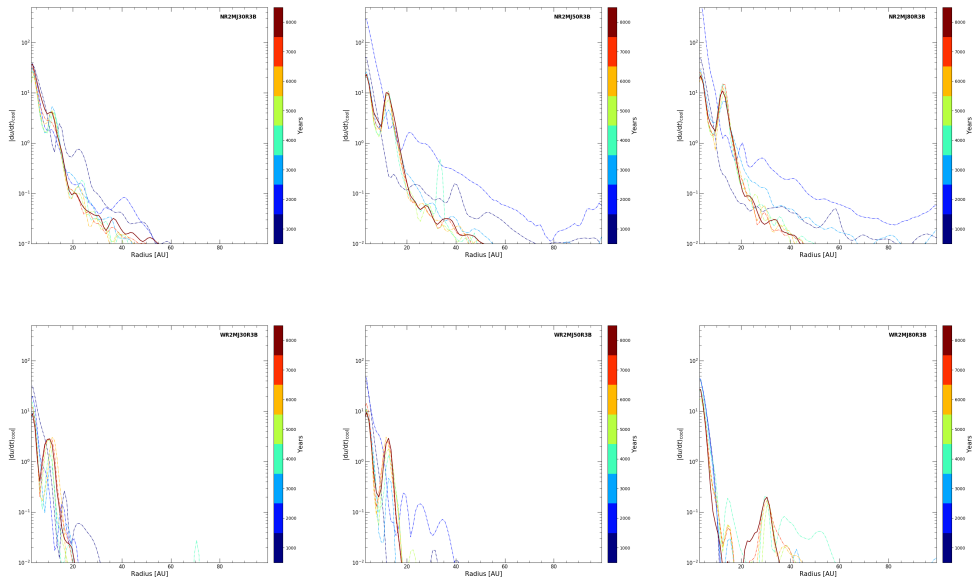

Figure 7.16: Azimuthally averaged β-cooling rate $|\mathrm{d}u/\mathrm{dt}|_{\mathrm{cool}}$. we take account of stellar radiation and radiative feedback from planet if it is considered in model

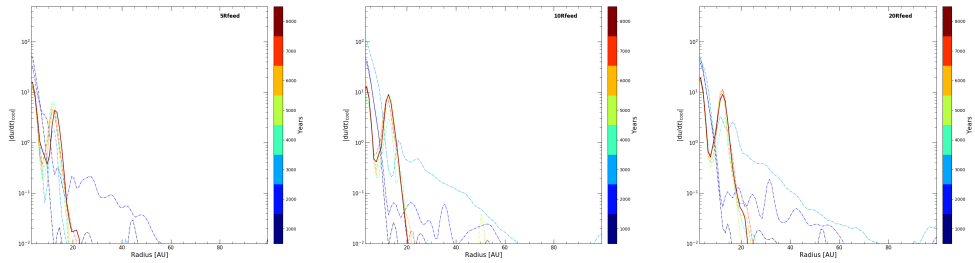

Figure 7.17: Azimuthally averaged β-cooling rate $|\mathrm{d}u/\mathrm{dt}|_{\mathrm{cool}}$. we take account of stellar radiation and radiative feedback from planet if it is considered in model

7.2 Tables

Table 7.1: Parameter space of paper simulations without planet radiation, Model ID is named: NR – No planet radiation, ∘∘MJ – Initial mass of planet in M_{J}, ∘∘R – Initial orbital separation in AU, ∘∘B – β coefficient

Model ID	Initial orbital separation (AU)	Initial mass (M_{J})	β coefficient	Radiative feedback radius ($R_{\odot}$)
NR2MJ60R1B	60	2	1	No radiation
NR2MJ60R10B	-	-	10	-
NR05MJ60R3B	60	0.5	3	No radiation
NR2MJ60R3B	-	2	-	-
NR5MJ60R3B	-	5	-	-
NR2MJ30R3B	30	2	3	No radiation
NR2MJ50R3B	50	-	-	-
NR2MJ80R3B	80	-	-	-

Table 7.2: Parameter space of paper simulations with planet radiation, Model ID is named: WR – With planet radiation, ∘∘MJ – Initial mass of planet in $M_{\rm J}$, ∘∘R – Initial orbital separation in $\rm AU$, ∘∘B – β coefficient

Model ID	Initial orbital separation (AU)	Initial mass ($M_{\rm J}$)	β coefficient	Radiative feedback radius ($R_\odot$)
WR2MJ60R1B	60	2	1	1
WR2MJ60R10B	-	-	10	-
WR05MJ60R3B	60	0.5	3	1
WR2MJ60R3B	-	2	-	-
WR5MJ60R3B	-	5	-	-
WR2MJ30R3B	30	2	3	1
WR2MJ50R3B	50	-	-	-
WR2MJ80R3B	80	-	-	-

Table 7.3: Parameter space of paper simulations varying feedback radius ($R_{\rm feed}$), Model ID is named: SM – Standard model ($M_{\rm i} = 2\,M_{\rm J}$, $R_{\rm i} = 60\,\rm AU$, and $\beta = 3$), ∘∘Rf – Feedback radius in $\rm R_\odot$, ∘∘B – β coefficient

Model ID	Initial orbital separation (AU)	Initial mass ($M_{\rm J}$)	β coefficient	Radiative feedback radius ($R_\odot$)
SM5Rf3B	60	2	3	5
SM10Rf3B	-	-	-	10
SM20Rf3B	-	-	-	20

Bibliography

[1] ALMA Partership, 2015, ApJ, 808, L3

[2] Andrew S. M., Wilner D. J., Hugues A. M., Qi C., Dullemond C. P., 2009, ApJ, 700, 1502

[3] Ayliffe B. A., Bate M. R., 2008, MNRAS, 393, 49

[4] Bae J., Zhu Z., Hartmann L., 2017, ApJ, 850, 2

[5] Bae J., Zhu Z., 2018, ApJ, 859, 118

[6] Bae J., Zhu Z., 2018, ApJ, 859, 119

[7] Baehr H., Klahr H., 2015, ApJ, 814, 155

[8] Baruteau C., Meru F., Paardekooper S. J., 2011, MNRAS, 416, 1971

[9] Bate M. R., Lubow S. H., Ogilvie G. I., Miller K. A., 2003, MNRAS, 341, 213

[10] Boss A. P., 2017, ApJ, 836, 53

[11] Cha S. H., Nayakshin S., 2011, MNRAS, 415, 3319

[12] Chametla R. O., Sánchez-Salcedo F. J., Masset F. S., Hidalgo-Gámez A. M., 2017, MNRAS, 468, 4610

[13] Cloutier R., Lin M. K., 2013, MNRAS, 434, 621

[14] Crida A., Barteau C., Kley W., Masset F., 2009, A&A, 502, 679

[15] D'Angelo G., Lubow S. H, 2008, ApJ, 685, 560

[16] Deng H., Mayer L., Meru F., 2017, ApJ, 847, 1

[17] Fletcher M., Nayakshin S., Stamatellos D., Dehnen W., Meru F., Mayer L., Deng H., Rice K., 2019, preprint, arxiv:1901.08089

[18] Gammie C. F., 2001, ApJ, 553, 174

[19] Gárate M., Cudara J., Montesinos M., 2017, preprint, arxiv:1711.01372

[20] Gressel O., Nelson R. P., Turner N. J., Zegler U., 2013, ApJ, 779, 59

[21] Haworth T. J., Ilee J. D., Forgan D. H., Facchini S., Price D. J. et al., 2016, PASA, 33, 22

[22] Helled R., Anerson J. D., Podolak M., Schubert G., 2011, ApJ, 726, 15

[23] Hopkins P. F., 2014, MNRAS, 450, 53

[24] Hubber D. A., Batty C. P., Mcleod A., Whitworth A. P., 2011, A&A, 529, A27

[25] Hubber D. A., Walch S., Whitworth A. P., 2013, ApJ, 430, 3261

[26] Hubber D. A., Rosotti G. P., Booth R. A., 2017, MNRAS, 473, 1603

[27] Humphries R. J., Nayakshin S., 2018, MNRAS, 477, 593

[28] Juhász A., Rosotti G. P., 2017, MNRAS, 474, L32

[29] Kley W., Bitsch B., Klahr H., 2009, A&A, 506, 971

[30] Kley W., 2012, ARAA, 50, 211

[31] Lubow S. H., D'Angelo G., 2006, ApJ, 641, 526

[32] Lubow S. H., Ida S., 2010, preprint, arxiv:1004.4137

[33] Machida M. N., Inutsuka S. I., Matsumoto T., 2006, ApJ, 649, L129

[34] Malik M., Meru F., Mayer L., Mayer M., 2015, ApJ, 802, 56

[35] Mercer A., Stamatellos D., 2017, MNRAS, 465, 2

[36] Mercer A., Stamatellos D., Dunhill A., 2018, MNRAS, 478, 3478

[37] Miranda R., Rafikov R. R., 2018, preprint, arxiv:18111.09628

[38] Nayakshin S., 2010, MNRAS, 408, L36

[39] Nayakshin S., Cha S. H., 2013, MNRAS, 435, 2099

[40] Nayakshin S., 2015a, MNRAS, 454, 64

[41] Nayakshin S., 2015b, preprint, arxiv:1502.07585

[42] Nayakshin S., 2017a, MNRAS, 470, 2387

[43] Nayakshin S., 2017b, PASA, 34, e002

[44] Nayakshin S., 2018, preprint, arxiv:1808.05151

[45] Rafikov R. R., 2002, ApJ, 569, 997

[46] Rafikov R. R., 2017, ApJ, 837,14

[47] Rice W. K. M., Armitage P. J., Bate M. R., Bonnell I. A., 2003, MNRAS, 339, 1025

[48] Rice W. K. M., Lodato G., Armitage P. J., 2005, MNRAS, 364, L56

[49] Sano T., Miyama S. M., 1999, ApJ, 515, 776

[50] Sch$'$afer C., Speith R., Hipp M., Kley W., 2004, A&A, 418, 325

[51] Semonov D., Henning T., Ilgner M., Sedlmayr E., 2003, A&A, 410, 611

[52] Spiegel D. S., Burrows A., Milsom J., 2011, ApJ, 727, 57

[53] Stamatellos D., Whitworth A. P., Bisbas T., Goodwin S., 2007 , A&A, 475, 37

[54] Stamatellos D., Whitworth A. P., 2008 , A&A, 480, 879

[55] Stamatellos D., Whitworth A. P., 2009, MNRAS, 400, 1563

[56] Stamatellos D., Whitworth A. P., Hubber D. A., 2011, ApJ, 730, 32

[57] Stamatellos D., Whitworth A. P., Hubber D. A., 2012, MNRAS, 427, 1182

[58] Stamatellos D., 2015, ApJ, 810, 1

[59] Stamatellos D., Inutsuka S. I., 2018, MNRAS, 477, 3110

[60] Szuágyi J., Morbidelli A., Crida A., Masset F., 2014, ApJ, 782, 65

[61] Szuágyi J., 2017, ApJ, 842, 103

[62] Tanaka H., 2002, ApJ, 565, 1257

[63] Tanakawa T., Ohtsuki K., Machida M., 2012, ApJ, 747, 47

[64] Toomre A., 1963, ApJ, 139, 1217

[65] Uribe A. L., Klahr H., Henning T., 2013, ApJ, 769, 9

[66] Val-Boore M., Edgar R. G., Artymowicz P., Ciecielag P., Cresswell P., D'Angelo G., Delgado-Donate E. J., Dirksen G., Fromang S., Gawryszczak A., Paardekooper S. J., Peplinski A., Pierens A., Plewa T., Rice K., Sch´afer C., Speith R., 2006, 370, 529

[67] Ward W. R., Canup R. M., 2010, ApJ, 140, 1168

[68] Wardle M., 2007, ARSS, 311, 35

[69] Williams J. P., Cieza L. A., 2011, ARSS, 49, 67

[70] Xu W., Goodman J., 2018, MNRAS, 480, 4327

[71] Zhu Z., Hartmann L., Nelson R. P., Gammie C. F., 2012, ApJ, 746, 110

[72] Zhu Z., 2015, ApJ, 799, 16

[73] Zhu Z., Ju W., Stone J. M., 2016, ApJ, 832, 18

초 록

무거운 원시행성계원반의 중력불안정으로 형성되는 목성형 행성은 주변 물질을 강착하면서 질량을 증가하고 원반과 조력 상호작용을 통해 이주한다. 힐 구 내의 냉각이 효율적일수록 흡착이 빨라지기에 행성 이주는 행성 질량과 원반의 냉각률에 직접적인 영향을 받는다. 목성형 행성의 형성과 진화를 다룬 수치 연구에선 목성형 행성이 갈색왜성 혹은 낮은 질량의 별로 진화한다는 결론을 냈다. 따라서 본 연구는 GIZMO (Hopkins 2015)를 이용해 3차원 유체역학 계산을 수행하여 무거운 원시행성계원반 내 목성형 행성 진화과정을 조사하고, 강착률에 상응하는 행성의 복사 되먹임을 고려했다. 복사과정은 β 냉각 모델 (Gammie 2011)로서 규정했다.

우리는 무거운 원시행성계원반에 존재하는 행성은 빠르게 안쪽으로 이주하면서 원반에 틈을 벌려 점차 이주를 멈추는 것을 확인했다. 차가운 원반 내에 무거운 행성이 존재할수록, 원반 물질이 힐 구 안으로 쉽게 축적될 수 있었고, 밀집한 행성 주변부원반을 형성해 높은 강착률을 보였다. 의미 있는 결과로는 일반적인 경우의 행성의 질량 성장이 갈색왜성 영역 밑에 존재한다는 점이다. 복사 되먹임의 존재는 행성의 질량 성장을 약화하고, 원반 내 틈 형성을 늦추었다. 본 논문은 다른 수치 연구들과의 비교를 통해 GIZMO를 이용한 결과를 논하고, 더 나아가 관측치와 행성의 진화 사이의 관계를 원반 내 틈, 나선무늬, 그리고 행성의 광도로서 설명한다.

주요어: 수치 실험: 유체역학 — 복사 되먹임,
원시행성계원반: 행성 — 행성-원반 상호작용 — 행성 이주
학번: 2016-23078